Repeating Low Frequency Icequakes in the Mont-Blanc Massif Triggered by Snowfalls

Agnès Helmstetter

JGR Earth Surface

RESEARCH ARTICLE
10.1029/2022JF006837

Repeating Low Frequency Icequakes in the Mont-Blanc Massif Triggered by Snowfalls

Agnès Helmstetter[1]

[1]ISTerre, Univ. Grenoble Alpes, Univ. Savoie Mont Blanc, CNRS, IRD, Univ. Gustave Eiffel, Grenoble, France

Key Points:

- I detected low frequency icequake signals with a main frequency of 5 Hz that repeat every few minutes
- Low frequency icequakes mainly occur during and after snowfall episodes
- They are located on several glaciers of the Mont-Blanc massif mainly above 3,000 m a.s.l. where the basal ice is possibly cold

Correspondence to:

A. Helmstetter,
agnes.helmstetter@univ-grenoble-alpes.fr

Citation:

Helmstetter, A. (2022). Repeating low frequency icequakes in the Mont-Blanc massif triggered by snowfalls. *Journal of Geophysical Research: Earth Surface*, *127*, e2022JF006837. https://doi.org/10.1029/2022JF006837

Received 12 JUL 2022
Accepted 23 NOV 2022

Abstract Deformation mechanisms of glaciers are highly sensitive to basal temperature; the motion of temperate glaciers is dominated by basal slip while cold-based glaciers deform mainly by internal creep. While basal slip is usually aseismic, unstable slip sometimes occurs and can be detected by seismometers. I have detected clusters of repeating low-frequency icequakes (LFIs) in the Mont-Blanc massif. Some properties of LFIs are similar to the high-frequency icequakes (HFIs) located at the base of Argentière glacier (Helmstetter, Nicolas, et al., 2015, https://doi.org/10.1002/2014jf003288). Both HFIs and LFIs occur as bursts of tens to several thousand events lasting for days or weeks, with typical inter-event times of several minutes during bursts. Unlike HFIs that have a broad spectra, LFIs have a characteristic frequency of about 5 Hz at all stations, suggesting a rupture length of about 100 m. Seismic amplitudes and seismic waveforms of LFIs progressively evolve with time within each cluster, suggesting changes in either rupture length or rupture velocity. Most LFIs are detected during snowfall episodes while HFIs are not correlated with snowfall episodes. In this study, I used all available seismic stations within or around the Mont-Blanc massif between 2017 and 2022. I found LFIs located all over the massif but mainly above 3,000 m. Some clusters are clearly associated with cold basal ice (near Mont-Blanc summit) while others below 2,700 m a.s.l. are likely located under temperate glaciers and two clusters could be associated with landslides. This observation of LFIs on cold glaciers is consistent with laboratory friction experiments suggesting that cold ice promotes unstable slip (McCarthy et al., 2017, https://doi.org/10.1098/rsta.2015.0348; Saltiel et al., 2021, https://doi.org/10.1785/0220200480; Zoet et al., 2013, 2020, https://doi.org/10.1002/jgrf.20052, https://doi.org/10.1029/2020gl088964).

Plain Language Summary Glaciers flow due to slip at the base of the glacier and due to internal deformation. When the ice is at the melting point temperature, the presence of water at the base of the glacier promotes basal slip, while for cold ice (below melting temperature) the glacier is stuck to its bed and most deformation occurs within the glacier. The displacement of the glacier is usually slow and continuous, but in some cases slip can occur as intermittent fast slip events. These "icequakes" generate ground vibrations that can be recorded by seismic sensors. In this study, I analyze clusters of icequakes that repeat more or less regularly with time every few minutes, with progressive changes in amplitudes and inter-event times. The signals have a narrow spectrum with a main frequency of about 5 Hz that suggests a rupture length of about 100 m. These events mainly occur during snowfall episodes and are mostly located on glaciers above 3,000 m. At these locations, the ice is often colder than the melting point temperature. These repeating icequakes are probably associated with unstable slip at the base of glaciers. This result is surprising since basal motion for cold ice (below melting point) is believed to be negligible, but it is however consistent with laboratory experiments suggesting that unstable slip is promoted by cold temperatures. A few events occur on or close to glaciers at lower elevations, where ice is at the melting point temperature. They may be associated with basal glacier motion or with landslides induced by glacier retreat.

1. Introduction

Basal icequakes have been observed under very different settings (ice-streams, outlet glaciers, alpine glaciers, and ice-clad volcanoes), with hard beds or basal till, over a huge range of scales (1 m–200 km), rupture durations (from 0.1 s to 30 min), frequency content (from 100 s to 500 Hz) and magnitudes ($-4 < m < 7$; see Podolskiy and Walter (2016) for a review). While most of these events have a high waveform similarity and occur more or less regularly in time, these events also tend to display progressive changes in amplitude and recurrence times (Allstadt & Malone, 2014; Helmstetter, Nicolas, et al., 2015; Röösli et al., 2016). Other processes generate seismic signals on glaciers, such as crevasse opening, collapsing séracs, water flow, snow avalanches or rockfalls. But, these signals do not repeat regularly in time like basal icequakes and they have a wider size distribution

(e.g., Helmstetter, Moreau, et al., 2015). Repeating basal icequakes are generally associated with stick-slip shear motion at "sticky-spots" at the ice-bed interface. The rupture area is stuck except during dynamic rupture (slip events). Stress decreases during slip events and increases between events due to aseismic deformation. The nature of "sticky-spots" is difficult to identify. They could be associated with rock debris sliding over hard bedrock (Helmstetter, Nicolas, et al., 2015) or with the plowing of clasts embedded in the base of the ice through wet low diffusivity till (Barcheck et al., 2018). Another common point is that most of these events occur under glaciers or ice streams with a temperate basal ice layer (ice at the melting point temperature), allowing aseismic slip around the "sticky-spot" to reload the asperity between events.

Glacier basal motion is mainly controlled by the temperature of the basal layer and by the nature of the bed (K. Cuffey & Paterson, 2010). For temperate-based glaciers, basal motion accounts on average for half of the total motion. Basal motion is due to slip on the ice-bed interface for hard beds, while for soft beds most basal motion is due to shear within the till layer. In contrast, cold glaciers with a basal layer below the melting point are believed to deform mainly by viscous creep within the bulk of the glacier, with negligible basal slip because ice is frozen to the bed (with a few contrasting studies, e.g., Echelmeyer and Zhongxiang (1987) and Cuffey et al. (1999)).

The mechanisms responsible for stick-slip events are still debated. While basal seismicity has mainly been observed so far for temperate basal ice, most laboratory friction experiments that reproduced unstable slip ("velocity-weakening" behavior) were using ice samples below the freezing temperature (McCarthy et al., 2017; Saltiel et al., 2021; Zoet et al., 2013, 2020). Basal icequakes can be triggered or modulated by tides (Bindschadler et al., 2003; Wiens et al., 2008), snowfalls (Allstadt & Malone, 2014; Thelen et al., 2013) and changes in basal water pressure (Röösli et al., 2016). Basal stick-slip motion is thus particularly informative of glacier sliding processes and of basal properties (Barcheck et al., 2018; Kufner et al., 2021; Smith, 2006).

In this study, I report observations of repeating icequakes in the Mont-Blanc area between October 2017 and June 2022. Repeating high frequency icequakes, with a mean frequency above 100 Hz, have previously been detected under Argentière glacier in the Mont-Blanc massif (Gimbert et al., 2021; Helmstetter, Nicolas, et al., 2015). These events were associated with the repeated failure of rock debris over the bedrock. This study describes another type of repeating icequakes, with a much lower average frequency of about 5 Hz. Both types of repeating icequakes occur as bursts of events lasting for a few days or weeks. During each burst, the time between successive icequakes and icequake amplitudes progressively evolve with time. But, unlike high frequency icequakes (HFIs), low-frequency repeating icequakes (LFIs) occur mainly during or after snowfall episodes. They also occur at higher elevations, possibly associated with cold-based glaciers. These differences suggest that LFIs may be generated by a different physical mechanism than HFIs.

2. Study Area and Instrumentation

2.1. Mount-Blanc Massif and Argentière Glacier

The Mont-Blanc massif extends over three countries (France, Italy, and Switzerland), starts at 4,807 m above sea level (a.s.l.), and includes about 155 km^2 of glaciers. There are both temperate valley glaciers with ice at the melting-point temperature (e.g., Mer de Glace and Argentière glaciers), polythermal (e.g., Taconnaz and Tête Rousse glaciers) and cold glaciers (e.g., Glacier de la Verte, Glacier de l'Aiguille du Tacul, Col du Dôme). Mer de Glace is the longest glacier of the massif; it culminates at 4,248 m a.s.l. and flows down to about 1,600 m a.s.l. over a length of about 12 km. Argentière glacier is the second largest glacier of the massif, with a length of 10 km and a maximum thickness of about 400 m. This glacier is particularly interesting as it has been studied for several decades with measurements of surface displacement and basal slip (Vincent & Moreau, 2016), subglacial water flow discharge, mass balance and meteorological data (Vincent et al., 2009). In addition, several ground penetrating radar experiments, boreholes and seismic reflection studies provided accurate information on the topography of the bedrock and on the seismic wave velocities (Gimbert et al., 2021). Although our goal was initially to analyze icequake activity on Argentière glacier, I found out that most detected events did not occur on Argentière glacier but were distributed all over the Mont-Blanc massif.

Table 1
Characteristics of All Seismic Stations Used in This Study

Name	Network code	Time interval	Sensor	Cut-off frequency	Sampling rate (Hz)
B01		2017/10/4–2018/9/13	Geobit-C100-MK2	0.1 Hz	1,000
B02		2018/4/18–2019/2/4,	Geobit S 400C	1 Hz	1,000
		2019/7/16–2019/10/16,			100
		2019/12/6–2020/5/11			100
B03		2018/10/23–2019/3/22,	Geobit C100-MK2	0.1 Hz	1,000
		2019/3/23–2019/5/14,			100
		2019/6/25–2020/1/27			1,000
B04		2019/6/26–2020/1/25	Geobit C100-MK2	0.1 Hz	100
DOM		2021/7/2–2021/8/28	Geobit S-100 1C	4.5 Hz	800
MDG		2021/9/18–2021/12/18	Geobit C100 3C	4.5 Hz	100
AR001-100	ZO	2018/4/25–2018/5/31	Fairfield ZLand 3C	4.5 Hz	500
N11-35	1D	2019/12/5–2020/1/10	Fairfield ZLand 3C	4.5 Hz	250
CI17-CI23	XT	2018/11/11–2019/12/3	Trillium Horizon	0.008 Hz	100
CI18-CI20	8C	Since 2019/12/20	Guralp CMG40	0.025 Hz	200
MFERR	8D	Since 2019/5/28	Lennartz LE-3D	1 Hz	100
AMID2, VFER2	8D	Since 2019/12/4	Lennartz LE-3D	1 Hz	200
BLANC	GU	Since 2019/6/14	Trillium 40s	0.025 Hz	100
REMY, LSD, CIRO	GU	Since 2011	Trillium 40s	0.025 Hz	100
MRGE	IV	Since 2005/6/24	Trillium 40s	0.025 Hz	100
SEMOS	CH	Since 2013/6/18	EpiSensor ES-T	None	250
DIX, SENIN	CH	Since 2016/11/4	Streckeisen STS2	0.008 Hz	200
AIGLE, SALAN	CH	Since 2018	Streckeisen STS2	0.008 Hz	200
ILLEZ, FULLY	CH	Since 2018	Trillium Compact	0.008 Hz	100
GRYON	CH	Since 2002/10/2	Trillium 240s	0.004 Hz	200
OGSI	FR	Since 2016/6/15	Trillium Compact	0.05 Hz	200
RSL	FR	Since 2010/5/28	Trillium 120PA	0.008 Hz	100

Note. Data for network codes ZO, 1D, 8C, GU, IV, CH, and FR are freely available via Federation of Digital Seismograph Networks web services.

2.2. Seismic Stations

I used all available temporary and permanent seismic stations in the Mont-Blanc area. Table 1 gives the characteristics of each station used in this study. The stations inside the Mont-Blanc massif are shown in the map in Figure 1.

Several seismological experiments have been performed on Argentière glacier since 2017. A few seismic stations operated between October 2017 and May 2020 (stations B01-B04), with several gaps in the acquisition. The first station B01 was installed on Argentière glacier on 4 October 2017 (Nanni et al., 2020). Then station B02 was installed at 70 m depth in a borehole close to B01 on 20 April 2018, followed by B03 on 23 October 2018 and B04 on 26 June 2019.

Two other temporary seismic stations were in operation during summer or autumn 2021. Station DOM was located near Col du Dôme and station MDG on Mer de Glace.

Two temporary 1-month experiments with a larger number of sensors have been performed. From 20 April 2018 until 31 May 2018, the lower part of Argentière glacier was instrumented with a network of 98 seismometers (stations AR001-AR100). The preliminary results of this experiment have been described by Gimbert

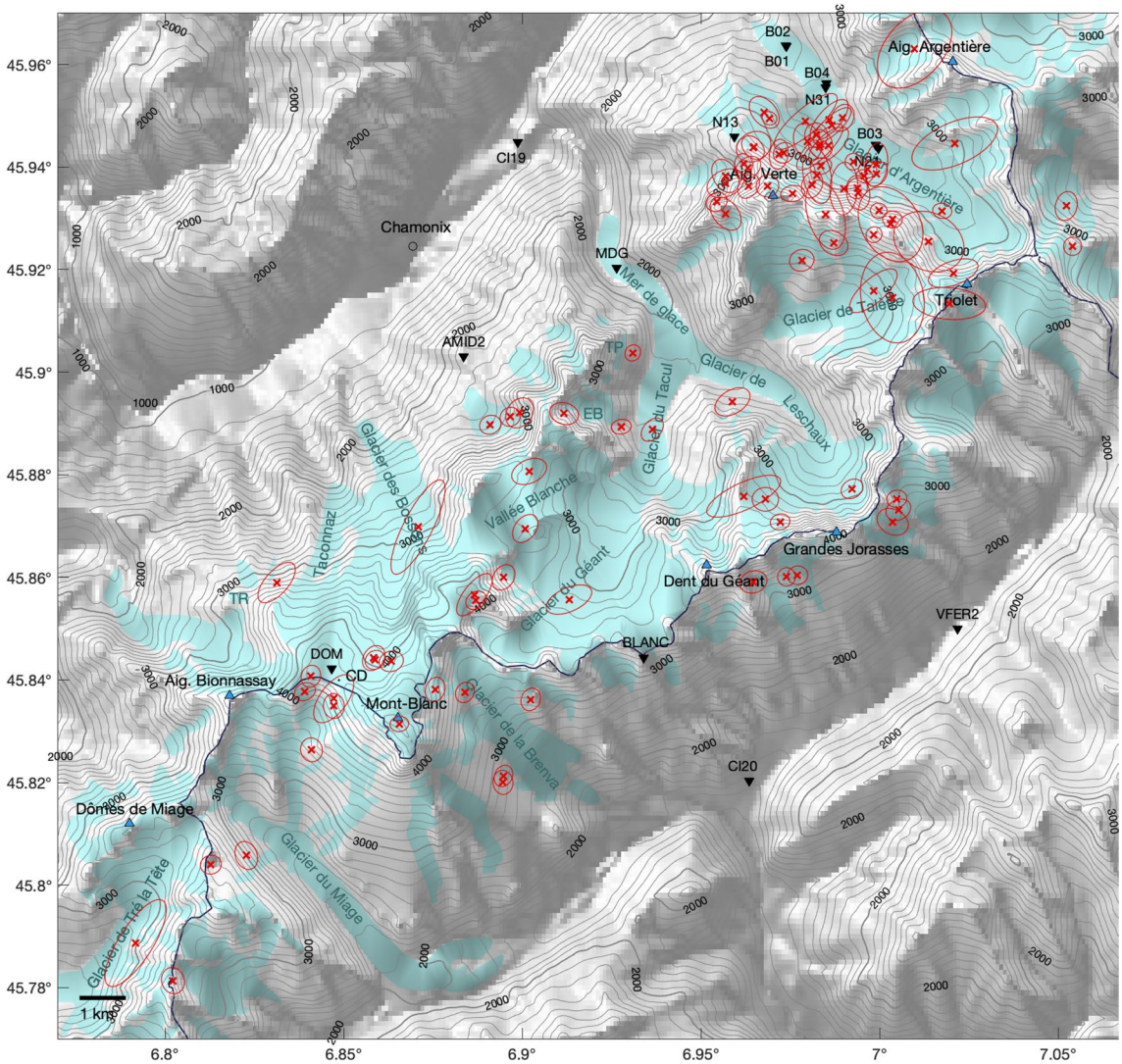

Figure 1. Map of the Mont-Blanc massif. Seismic stations are shown by black triangles. Gray lines show the topography, black lines are national boundaries and blue areas are glaciers. Small glaciers mentioned in the text: TR indicates Glacier de Tête Rousse, TP Glacier de Trélaporte, EB Glacier de l'Envers de Blaitière, CD Col du Dôme. Repeating low-frequency icequakes are shown by red crosses. Red lines show the horizontal error ellipses at the 68% confidence level.

et al. (2021) and the data are available from Roux et al. (2021). Another short-term experiment has been conducted from 5 December 2019 until 10 January 2020 using 13 sensors distributed in 3 small networks (Helmstetter & RESIF, 2020). A network of five sensors (N11-N15) was located at Col des Grands Montets at about 3,260 m a.s.l. with a distance between sensors of about 100 m. Another network of four sensors (N21-N24) was located near station B03 at about 2,650 m a.s.l. and the last network (N31-N34) was located near B04 at about 2,500 m a.s.l. All these sensors lost their GPS signal after being started in Chamonix on 4 December 2019 and before installation on the glacier the next day. I was not aware that these sensors should not be moved after acquisition starts. I thus used local earthquake signals in order to correct the clock drift, which reached about 1 s after 1 month. I found a timing accuracy of about 0.02 s, which is not sufficient to use beam-forming methods but has little impact on the location results shown in Figure 1 because the timing error is much smaller than the average time residual. I thus selected only one sensor (N13, N21, or N31) out of each network.

Station BLANC was installed within the Mont-Blanc massif near Torino Refuge at an elevation of 3,379 m on 14 June 2019. I also used data from stations around the Mont-Blanc massif. Stations CI17-CI23 of the CIFALP project (Zhao et al., 2018) were in operation between 11 November 2018 and 3 December 2019. Stations CI18-CI20 were reinstalled at the same location on 20 December 2019 (Helmstetter et al., 2020). Three stations

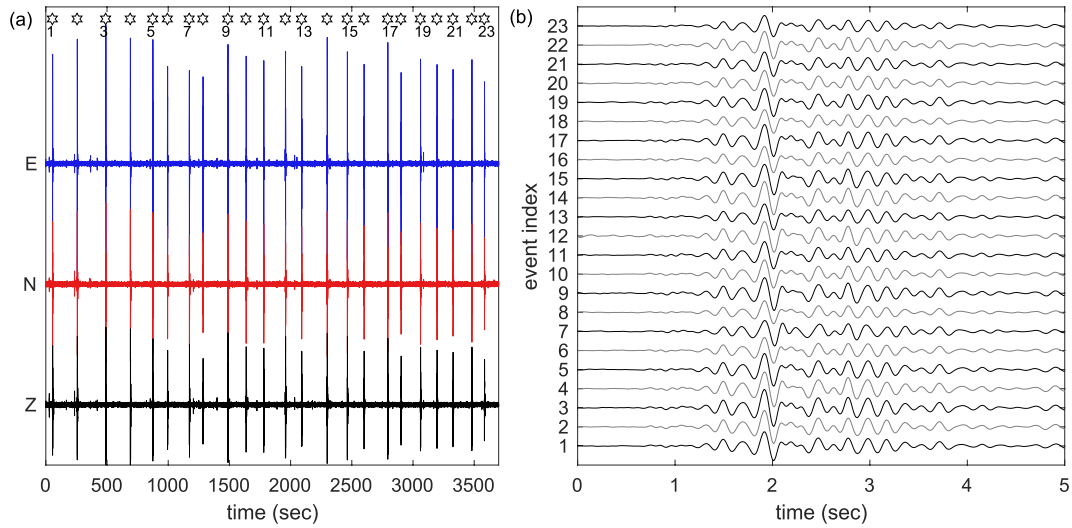

Figure 2. (a) Seismic signal recorded by station B01 on 19 December 2017 at 22:00 UTC bandpass filtered between 1 and 20 Hz. Low-frequency icequakes are highlighted by stars. The corresponding seismograms for each event are shown in panel (b) for the East component.

(MFERR, VFER2, and AMID2) were installed by ETH Zurich in 2019 to detect and locate earthquakes in the Mont-Blanc massif. I also used permanent seismic stations located further away from the Mont-Blanc massif, from the Switzerland Seismological Network (Swiss Seismological Service, 1983), the network of North Western Italy (University of Genova, 1967), the INGV Seismological Data Centre (INGV, 2006), and the French broadband network (RESIF, 1995).

2.3. Snowfalls and Atmospheric Pressure

I used meteorological data to analyze the influence of precipitation and atmospheric pressure on the occurrence of LFIs because snowfalls have been suggested to trigger icequakes (Thelen et al., 2013). A permanent meteorological station is installed on a moraine above Argentière glacier near 2,400 m a.s.l. as part of GLACIOCLIM observatory (Six & Vincent, 2014). However, this station does not measure snowfall. The closest station that measures snowfall is a Meteofrance station located outside the Mont-Blanc massif, in the Aiguilles Rouges massif, at 2,365 m a.s.l. But, there are many gaps in the snowfall data during snowfall episodes. Therefore, I use data from the S2M database (Vernay et al., 2019), which provides a reanalysis of meteorological and snow cover data. This model adjusts an estimate from a numerical weather prediction model with the best possible set of available in-situ meteorological observations. It provides the hourly rate of snowfall on the Mont-Blanc massif for different ranges of elevations and slope orientations.

The GLACIOCLIM station has only measured atmospheric pressure since 13 September 2019. Before this date, I use data from the closest Meteofrance station that measures atmospheric pressure located at Bourg Saint Maurice, 24 km south of Mont-Blanc. I checked that both stations provide similar values after shifting the Bourg Saint Maurice pressure to correct for the effect of elevation. When both stations are in operation the correlation coefficient between the pressure measured at Argentière and Bourg-Saint-Maurice is 0.88.

3. Methods

3.1. Detection, Classification, and Selection of Repeating LFIs

I detected a first sequence of low-frequency icequakes by simply looking at a 1-hr long signal recorded by station B01 on 19 December 2017 starting at 22:00 UTC. In Figure 2, we can see very regular peaks in the seismogram repeating on average every 160 s. Signals are highly similar, with a duration of about 5 s, an average frequency around 5 Hz and no high frequency energy. Once we identify one event, it is straightforward to detect similar events using the template-matching method (Gibbons & Ringdal, 2006). I first used this method with a relatively

low correlation threshold (0.4), a time window of 5 s, a bandpass filter of 2–20 Hz, and using the three components of station B01. By screening the waveforms of detected events, I noted significant and abrupt changes in the waveforms and amplitudes. I thus divided the set of detected events into different clusters using the hierarchical agglomerative clustering method with average linkage (Sokal & Michener, 1958).

In order to perform a more systematic detection, I applied the STA/LTA algorithm of Allen (1978) on all the data at the reference station using a signal-to-noise ratio of 3, a short-time window of 1 s, a long-time window of 20 s and a bandpass filter between 3 and 10 Hz. I used different reference stations for different periods: B01 (4 October 2017–12 June 2018), B03 (23 October 2018–11 September 2019), N21 (5 December 2019–10 January 2020), B02 (8 February 2020–12 May 2020), and BLANC (14 June 2019–1 June 2022). I detected on average more than 300 events per day, with a large variability in amplitude, frequency content and signal duration, likely produced by different processes (crevasse opening, basal slip, avalanches, rockfalls, earthquakes, noise…). The number of detected events was much too large (several hundred thousand events) to apply the hierarchical clustering method in order to group events into clusters with similar waveforms. I thus screened the time series of event times and amplitudes to identify bursts of events with similar amplitudes and duration and quasi-periodic recurrence times. I also applied the hierarchical clustering method on all large events (peak ground velocity larger than 10 μm/s) to make sure that I did not miss any cluster of large amplitude signals.

In this way, I identified several thousand clusters of low-frequency signals for the whole time period. Within each identified cluster, I computed the average signal and used this stacked signal as the new template signal for this cluster. When the correlation between different templates was larger than 0.9, I merged the clusters. I then applied the template-matching algorithm on the continuous data at the reference stations with a correlation threshold of 0.5. I used different signal durations for different clusters (2, 3, or 5 s), starting about 0.5 s before the first arrival and ending just after the last visible arrival. If an event was detected by several templates, I chose the one with the largest correlation.

In this work, I am interested in detecting "low-frequency" repeating icequakes (LFIs) similar to those shown in Figure 2. Here, the term "low-frequency" means average frequency of about 5 Hz, much lower than the average frequency of about 50 Hz for the HFIs located below the lower part of Argentière glacier near 2,350 m a.s.l. (Gimbert et al., 2021; Helmstetter, Nicolas, et al., 2015). The definition of "repeating" events is also non-trivial (Uchida & Bürgmann, 2019). Here I consider repeaters as events occurring quasi-periodically in time, that is, that are more regular than a Poisson random process (with uniform rate in time). I do not impose that they rupture the same asperity, because the uncertainty in location is comparable to the rupture length.

Regularity in time is usually characterized by the coefficient of variation (ratio of standard deviation over average recurrence time), with a value equal to 1 for a Poisson process, smaller than 1 for quasi-periodic occurrence times and larger than one for temporally clustered events. But, the coefficient of variation does not provide a good way to identify repeating icequakes. Repeating LFIs occur as bursts of activity followed by quiescent periods, as observed before for HFIs (Helmstetter, Nicolas, et al., 2015). During active periods, both the inter-event times and the amplitude evolve progressively in time. The coefficient of variation is thus often larger than one, due to the succession of active phases and periods of very low activity (possibly misclassified events) and to progressive changes in recurrence time. To account for slow changes in activity rate, I normalize each recurrence time by the median value over a sliding window of 10 events. I also replace the standard deviation by the median absolute deviation, which is less sensitive to extreme events. Our modified "coefficient of variation" is thus defined as $median(|dt^* - 1|)$, where dt^* is the normalized recurrence times. I select all clusters with a coefficient smaller than 0.5, significantly smaller than values in the range 0.6–0.7 obtained for Poissonian synthetic catalogs.

During quiet phases between bursts of LFIs, events usually have a smaller correlation with the template than during bursts for the same peak amplitude. These isolated events may thus have a slightly different location or be due to a different triggering factor. I thus remove these isolated events before attempting to locate them or to analyze the correlation with potential triggering factors. For each cluster of repeaters, I remove events with inter-event times larger than 10 times the median value. A cluster is thus divided in several temporal sub-clusters, separated by gaps longer than 10 times the median inter-event time. In order to limit the number of sub-clusters, I then merge together sub-clusters if the gap is less than 1/4 of the duration of the smallest sub-cluster.

3.2. Localization

3.2.1. Stacking and Picking Signals

I attempted to locate each cluster of LFIs by manually picking P and S phases at a maximum of stations. Since individual events are rarely visible at stations outside the glacier, I stacked the signals for a selection of events for each cluster. For large clusters with more than 1,000 events, I selected only the 1,000 best events, with the largest amplitude and correlation with the template signal at the reference station. For all clusters I selected events that occurred during the bursts (i.e., more active phases), because events that occurred isolated in time during quiet periods are more likely to be false detections and to come from a different source. Signals were first bandpass filtered between 2 and 20 Hz. Instead of using the average, I used the median signal at each time sample over all selected events because it improves the signal-to-noise ratio by removing the influence of outliers (Allstadt & Malone, 2014). This helps to reduce the influence of noisy signals or false detections. Before taking the median, I removed events with a very large noise amplitude, for example, due to anthropogenic noise, instrumental issues or noise due to water flow. I computed the average noise amplitude over a time window of 20 s before each event and removed events with a noise amplitude larger than twice the median value.

I then manually picked first arrivals of P and S waves at all available stations listed in Table 1 when I could visually identify these phases. For the three networks of nodes (N11–N15, N21–N24, and N31–N34) installed in December 2019, I selected only one station for each network (nodes N11, N21, and N31). Because of the small inter-node distance (about 100 m), large source-node distance (several kms) and clock errors for these stations, I believe including more sensors would not improve the location accuracy. In order to keep only the best constrained locations, I selected only clusters with a minimum of seven phases picked at a minimum of four stations and also imposed at least one station outside the glacier. I did not use data from the nodes AR001–AR100 installed in April–May 2018 during the Resolve experiment. These nodes detected only two clusters of LFIs but these clusters could not be located accurately because they were not detected by stations outside the glacier.

3.2.2. Velocity Model

Tomographic studies in the Alps do not have a good enough resolution and are not adapted to this study of shallow sources because they do not estimate seismic wave velocity above sea level. Therefore, I used phase arrivals from swarms of micro-earthquakes in the Mont-Blanc area in order to estimate average P and S wave velocities. I selected 1,710 earthquakes detected by the regional seismological network Sismalp (https://sismalp.osug.fr) from 1 January 2017 until 27 January 2021 with latitude in the range 45.8°–46°N and longitude between 6.8° and 7.1°E. Most of these events were part of a swarm located below the Grandes Jorasses summit at about 5 km depth below sea level, while another smaller swarm was located under Aiguille du Midi. For each station in Table 1 and for each earthquake I computed apparent P and S velocities from earthquake source times and phase arrivals. I then took the average over all events at each station and then averaged over all stations. This yielded $V_P = 5.68$ km/s and $V_S = 3.41$ km/s. Since icequakes are quite shallow and located at a larger elevation than most stations, I account for the surface topography to avoid ray paths in the air. I use NASA SRTM digital elevation data with a resolution of 30 m (Jarvis et al., 2008). Our 3D velocity model is homogeneous below the surface and has $V_P = 0.34$ km/s and $V_S = 0.01$ km/s in the air. V_S needs to be positive in the air but its value has no influence on the results as long as $V_S \ll 1$ km/s. It covers the Mont-Blanc massif and extends further away to include all seismic stations listed in Table 1. The grid spacing is fixed to 100 m in all directions and the depth ranges between 0 and 5 km a.s.l. I cannot increase the resolution because the size of the 3D velocity model of dimension 5 km × 100 km × 100 km would be very large and the computing time too long.

Seismic wave velocities in the ice are significantly smaller than in the bedrock ($V_P = 3.62$ km/s, $V_S = 1.83$ km/s) (Gimbert et al., 2021). For stations located on glaciers, this can thus yield notable errors in the estimated travel times. However, the geometry of glaciers is not well known, except for Argentière glacier. But, I cannot include the ice layer in the velocity model due to its limited resolution in space (grid size of 100 m). I thus use station corrections to minimize these errors.

3.2.3. Station Corrections

Station corrections can account for un-modeled heterogeneities in the seismic wave velocities. Many stations are located on Argentière glacier above several hundred meters of ice. I estimated time corrections for these stations by computing travel-times in the velocity model described above ($V_P = 5.68$ km/s, $V_S = 3.41$ km/s below the

surface) and in a 3D model accounting for different velocities within Argentière glacier. The geometry of the glacier is defined by a synthesis of radar and seismic profiles (Gimbert et al., 2021). The seismic wave velocities in the ice ($V_P = 3.62$ km/s, $V_S = 1.83$ km/s) were inverted from the localization of high-frequency basal icequakes detected by the Resolve experiment (Gimbert et al., 2021). I then estimated travel times for each velocity model (with and without glacier) on a rectangular grid covering the Argentière glacier (longitude between 6.956° and 7.046°E, latitude between 45.913° and 45.97°N) with a grid spacing of 30 m, for each station on the glacier and for each grid point. The time delay between the two models varies in space but is relatively homogeneous outside the Argentière glacier and at large distance from the station. The time correction for each station is thus defined as the average time delay for grid points located at the surface outside the glacier and south-west from the glacier. I do not include grid points located within the northern part of the grid because I found very few icequakes in this area and because the time delay computed for station N13 (near Col des Grands Montets) is very different for points located south or north from Argentière glacier (i.e., for ray paths that do or do not cross the glacier). The maximum time delay of 0.14 s is obtained for S waves at station B04, where the glacier thickness is the largest reaching about 450 m.

3.2.4. Location Method

I use NonLinLoc location method (Lomax et al., 2000), which uses a probabilistic location method providing more accurate estimates of location errors. This method provides the most likely location as well as a scatter of possible solutions. This is particularly interesting when there are multiple local minima of time residuals. I use the 3D velocity model described above and station corrections for stations on the glacier. I assume Gaussian picking errors with a standard error of 0.1 s for both P and S waves and minimize the root-mean-square residuals. The inversion is performed using the Oct-tree Importance Sampling Algorithm as it is much faster than a grid-search. The topography of the area is used to search for possible sources located only below the ground surface.

3.3. Magnitude

Among all types of magnitudes, the moment magnitude is generally preferred as it directly depends on physical source properties, rupture area and slip. However, it is difficult to estimate moment magnitude for our signals because they have a limited frequency range, a very small signal-to-noise ratio for most events and for stations outside the Mont-Blanc massif, and are possibly dominated by surface waves. I thus estimated both the surface-wave magnitude M_s and the local magnitude M_l.

I used the definition of the surface-wave magnitude given by Bormann and Dewey (2014)

$$M_s = \log_{10}(A/2\pi) + 1.66\log_{10}\Delta + 0.3, \quad (1)$$

where A is the maximum amplitude of the surface-wave on the vertical trace and Δ is the epicentral distance in degrees. Note that I use this definition of M_s out of its recommended range of frequencies (3–60 s) and epicentral distance ($2° < \Delta < 60°$).

The local magnitude is given by (Bormann & Dewey, 2014)

$$M_l = \log_{10}(A_d) + 1.11\log_{10}(d) + 0.00189d - 2.09 + C, \quad (2)$$

where A_d is the amplitude in nm of the horizontal displacement seismogram that would have been recorded on a Wood-Anderson seismometer and d is the hypocentral distance (in km). This definition of M_l is only valid for crustal earthquakes in regions with attenuation properties similar to those of Southern California (Bormann & Dewey, 2014), I thus added a corrective term C. I estimated the correction term $C = 0.4$ to match the local magnitude of local earthquakes detected by Sismalp (https://sismalp.osug.fr) and computed using seiscomp software, for a selection of 30 earthquakes located in the Mont-Blanc massif with $0 < M_l < 3.1$ between 21 December 2018 and 23 January 2021.

Both types of magnitudes are not well adapted to this study. Local magnitude is generally used for seismic signals dominated by body waves, while M_s estimated from Equation 1 is recommended for lower frequencies and larger source-sensor distances. However, I used these magnitude scales because I did not find any other magnitude definition applicable to this type of signal.

For each cluster, I compute the magnitudes M_l and M_s of the largest event that occurred during active phases (rejecting isolated events). However, even the largest event is not always visible on all stations where this cluster was picked due to the weak signal-to-noise ratio. I thus applied the following procedure to estimate the amplitude A of the largest event at each station. For each station, I compute the amplitude A_i of each event i by computing the scaling amplitude factor between the signal y_i and the stacked signal y_s (Gibbons & Ringdal, 2006; Schaff & Richards, 2011)

$$A_i = A_s \frac{\sum_{j=1}^{N} y_i(t_j)\, y_s(t_j)}{\sum_{j=1}^{N} y_s(t_j)^2}, \tag{3}$$

where y_s is the vertical component of the stacked signal, A_s is its peak amplitude and the time index j varies from 2 s before until 2 s after the time of the peak amplitude of the stacked signal. This greatly improves the accuracy of the estimated peak amplitude for repeating signals, but is often still unreliable when the signal is buried in the noise. I thus fit a linear regression between the peak amplitude estimated at the reference station (B01, B02, B03, or BLANC) and at each other station, after selecting events that have a correlation with the stacked signal greater than its median value. This helps to remove noisy events and to obtain a more accurate value for the peak amplitude of the largest event of each cluster at each station.

4. Results

4.1. Characteristics of Seismic Signals

Many different types of icequakes have been detected on Argentière glacier (Gimbert et al., 2021; Helmstetter, Moreau et al., 2015; Helmstetter, Nicolas, et al., 2015), including repeating HFIs located at the base of the glacier at a few hundred meters from the sensor. HFIs have a much broader spectrum than the LFIs described in this study, with energy above 200 Hz. However, it is not clear whether the LFI frequency content represents the frequency of the source process or if the signal is strongly affected by attenuation that depletes the signal in high-frequencies.

Figure 3 compares the seismograms and spectra of low- and high-frequency repeating icequakes with a local earthquake recorded at station B01. The LFI signal has less energy above 6 Hz compared with a local earthquake of $M_l = 1.1$ detected at a distance of 10 km, whereas the LFI is located closer at about 3.5 km from the sensor.

Distinguishing the different phases for the LFI shown in Figure 3b is non-trivial. The different waves are more easily identified when bandpass filtering the data between 2 and 10 Hz, stacking over all events of the same cluster and looking at the signal polarization (see Figure 4). Large amplitude waves arriving after the S wave could be surface waves or scattered waves. Their polarization along the transverse direction suggests they could be Love waves.

4.2. Temporal Evolution

Clusters of repeating LFIs are generally active for a few hours or days. The same cluster (i.e., events with similar waveforms and therefore nearby locations) can however reappear a few days or months later. Figure 5 displays the temporal evolution of repeating events during one of the most active periods between 27 October 2018 and 9 November 2018. This figure only shows the seven clusters with at least 1,000 events during this time period. In addition, I also plot a smaller cluster of 190 events that displays a highly regular pattern and longer recurrence times (black dots in Figure 5). This cluster was located on the upper part of Glacier de Leschaux. Figure 5 illustrates the typical patterns as well as discrepancies between clusters. Clusters usually start as very small events with short and irregular occurrence times. But, during the beginning of the cluster many small events are likely missed. In a second phase, both the amplitudes and the recurrence times increase over time and become more regular. Some sequences then stop abruptly or slow down slowly with a progressive decrease in amplitudes and increase in recurrence times. I found no correlation between the LFI occurrence times between different clusters.

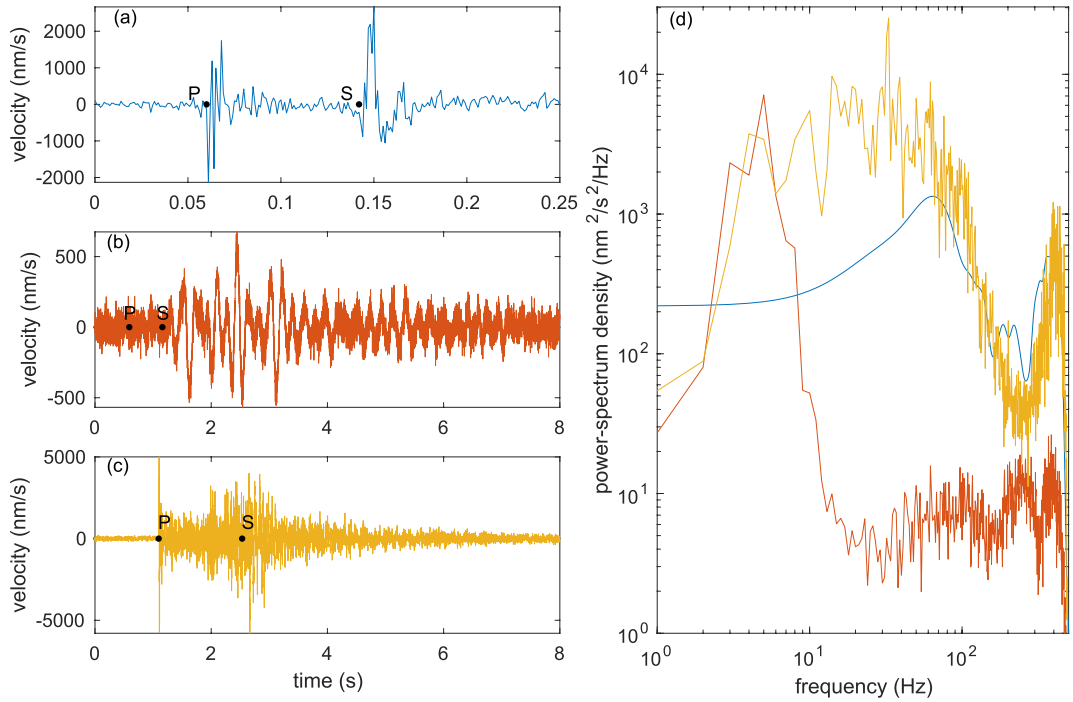

Figure 3. Seismograms of (a) a high-frequency icequake, (b) a low-frequency icequake (LFI), and (c) a $M_l = 1.1$ local earthquake detected at station B01. Signals are vertical ground motion high-pass filtered at 1 Hz. Arrival times of P and S waves are shown by dots. The corresponding spectra are shown in panel (d) for the high-frequency icequake in blue, LFI in red and local earthquake in yellow.

4.3. Correlation With Snowfall Episodes

Figures 6 and 7 compare the snow height and the snowfall rate with the rate of repeating LFIs for two time periods. Repeaters are mostly observed between October and May. Few events are observed in summer but they could be hidden by the increase in seismic noise during the melting period. Most bursts of repeaters coincide with snowfall episodes. LFIs are more frequent in autumn than in winter. The earlier snowfalls in November and December trigger more LFIs than latter similar snowfall episodes. The correlation between snowfalls and LFIs is confirmed by computing the cross-correlation between the snowfall rate and the rate of repeating events shown in Figure 8. The cross-correlation function shows a peak for positive times (icequakes occurring after snowfall episodes) with a maximum at 1.6 days and returns to zero after 10 days. Smaller and broader peaks for negative

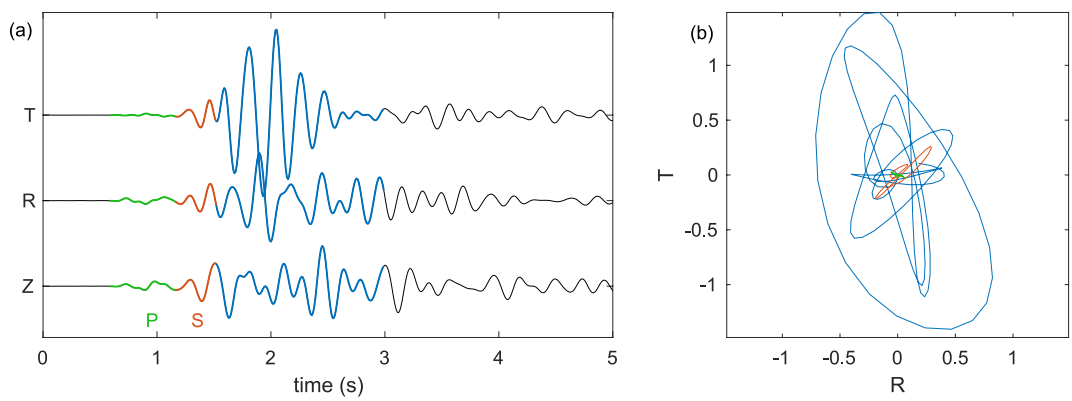

Figure 4. (a) Seismograms of the stacked signal for one cluster of low-frequency icequakes detected at station B01 bandpass filtered between 2 and 10 Hz. The signal has been rotated in the radial ("*R*") and transverse ("*T*") plane. (b) Velocity ground motion in the horizontal plane. *R*/*T*. P waves are shown in green and S waves in red. Later arrivals in blue are probably surface waves or scattered waves.

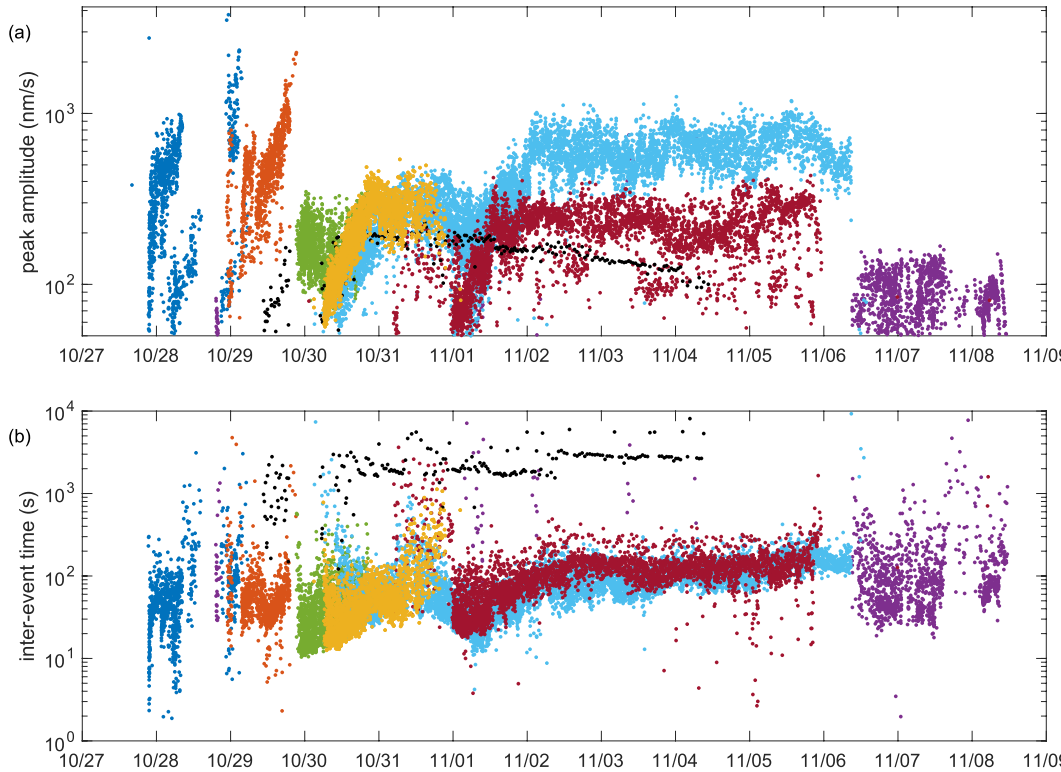

Figure 5. Temporal evolution of peak amplitude (a) and recurrence time (b) for a selection of 8 different clusters of repeaters between 27 October 2018 and 9 November 2018. Each color represents a different cluster.

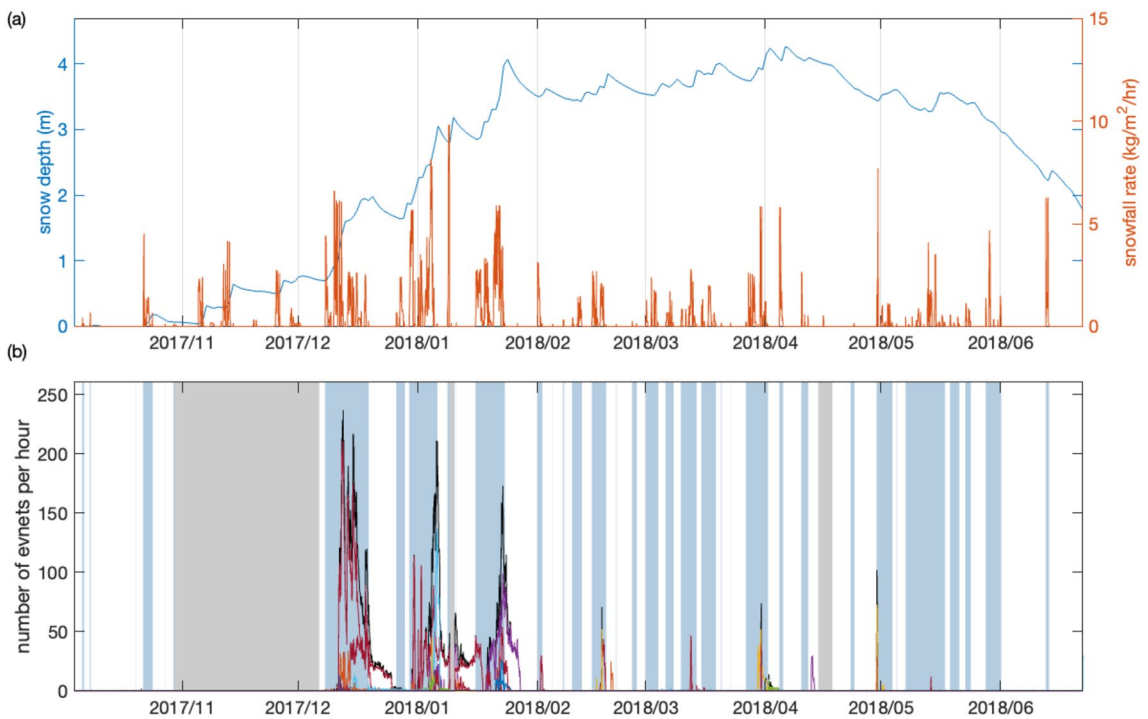

Figure 6. (a) Temporal evolution of snow depth and snowfall rate and (b) rate of repeating events detected at station B01. Blue shaded areas indicate snowfall episodes and gray areas data gaps. Different colors indicate different clusters. The black curve represents the sum over all clusters.

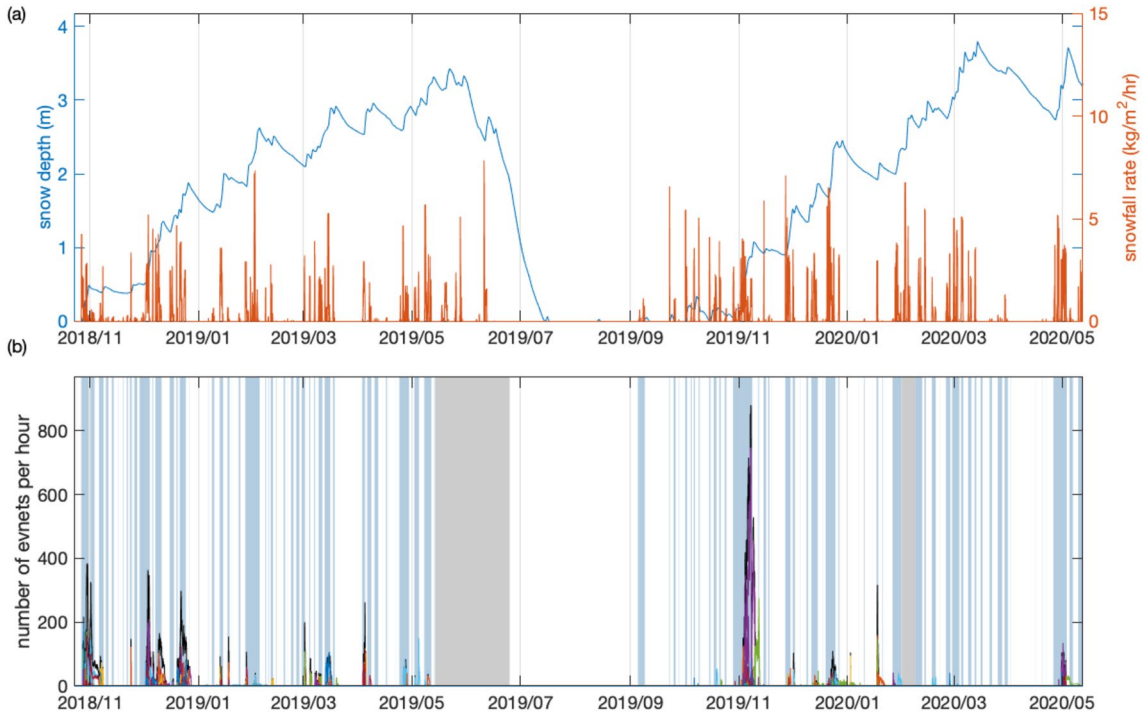

Figure 7. Same as Figure 6 for the time period 23 October 2018–12 May 2020. (a) Temporal evolution of snow depth and snowfall rate and (b) rate of repeating events detected at station B03 before 28 January 2020 and at station B02 after 28 January 2020.

times are spurious and result from peaks in the autocorrelation of snowfall rate. The hourly rate of LFIs is also negatively correlated with atmospheric pressure. This is surprising since decreasing the atmospheric pressure should have the same effect as decreasing the snow load. If snow load triggers LFIs, then increasing atmospheric pressure should also trigger LFIs. Atmospheric pressure is also strongly anti-correlated with snowfall rate (black curve in Figure 8) so that it is difficult to disentangle the relative effect of atmospheric pressure and snow load on the triggering of LFIs. Changes in atmospheric pressure and snow load have indeed the same order of amplitude. While the rate of LFIs is anti-correlated with atmospheric pressure, it is positively correlated with the hourly change in atmospheric pressure (green curve in Figure 8).

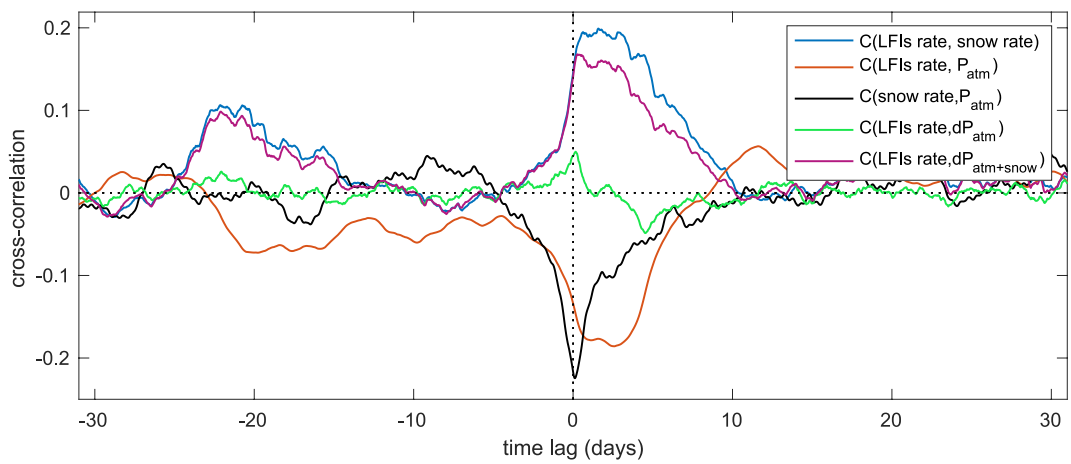

Figure 8. Normalized cross-correlation function between hourly rate of low-frequency icequakes (LFIs) for the time period 4 October 2017–12 May 2020 and snowfall rate in blue, between rate of LFIs and atmospheric pressure in red, between rate of LFIs and hourly change in atmospheric pressure in green, between rate of LFIs and total hourly pressure change (sum of atmospheric pressure change and snow rate) in purple, and between atmospheric pressure and snowfall rate in black.

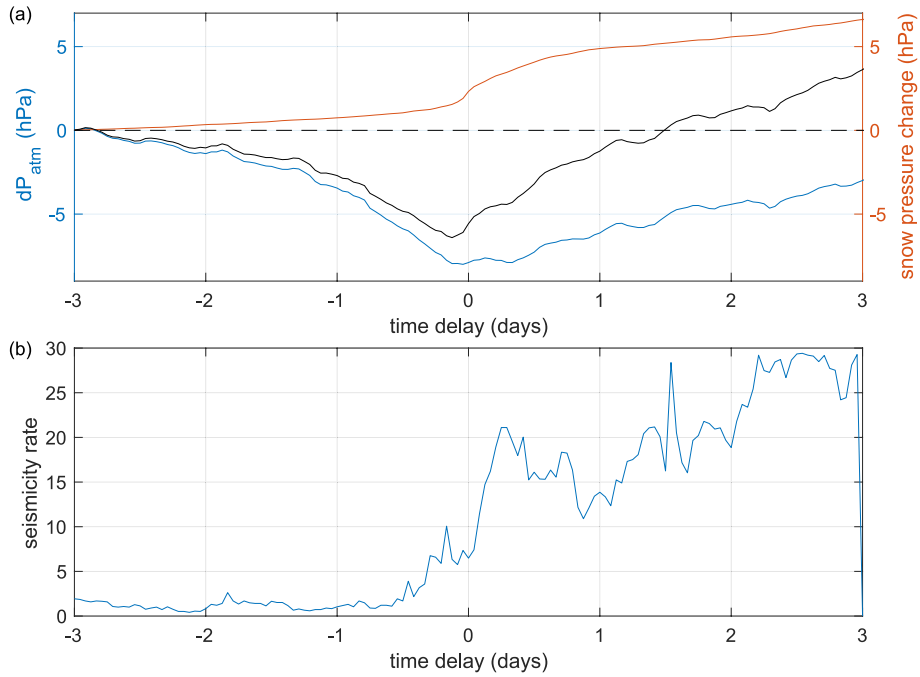

Figure 9. Average temporal evolution of (a) snow load in red, atmospheric pressure in blue, sum of these two terms in black and (b) rate of low-frequency icequakes, stacking over 29 selected snowfall episodes with a total pressure change larger than 1 hPa (corresponding to a snow load of 10 kg/m^2) and aligned in time relative to the peak of snowfall rate.

I have analyzed the average temporal evolution of atmospheric pressure, snow load and LFI rate during snowfall episodes. I selected 29 snowfall episodes with snow loads larger than 1 hPa that started at least 3 days after the end of the previous episode. I then stacked each variable for all snowfall episodes relative to the time of peak snowfall rate (see Figure 9). The results show that the snow load increases on average by 7 hPa 3 days after the peak of snowfall rate compared to its value 3 days before the peak. During the same time interval, atmospheric pressure decreases by 8 hPa and reaches its minimum value when the snowfall rate is maximum. It then recovers up to −3 hPa 3 days after the peak of snowfall rate. Summing snow load and atmospheric pressure, the average effect on normal stress change is thus positive for times larger than 1 day after the peak of snowfall rate. The increase in overburden also increases the basal shear stress, especially on steep slopes. The average rate of LFIs is larger than average for positive times, when both atmospheric pressure and snow load increase. Note however that this describes the average behavior but that individual sequences can differ widely from this typical pattern.

Figure 10 further confirms that LFIs occur predominantly during snowfall episodes, but also during times of low atmospheric pressure and when pressure increases. Figure 10 shows the probability distribution functions (pdfs) of atmospheric pressure, hourly atmospheric pressure change, and snowfall rate. It compares the pdfs at all times during seismic acquisition (blue curves) and at times of LFIs (red curves). LFIs are roughly two or three times more frequent than average during snowfall episodes and when atmospheric pressure is lower than 750 hPa. The hourly rate of LFIs is almost independent of the hourly snowfall rate, probably because of the time delay between snowfall rate and LFIs rate. The change in atmospheric pressure has a smaller impact on the occurrence of LFIs, with the rate of LFIs increasing by 21% when the atmospheric pressure increases (Figure 10b).

I also estimated the relation between the cumulated snow load during each snowfall episode and the number of LFIs (Figure 11). I defined snowfall episodes from the snowfall hourly data as consecutive days (24 hr) with a positive snowfall rate separated by at least 24 hr without snow. Clusters were separated into temporal sub-clusters as described in Section 4.1. For each snowfall episode, I selected sub-clusters that initiated after the beginning of the snowfall episode and I count all events of the sub-cluster until 10 days after the peak of snowfall rate, even after the end of the snowfall episode. Both the number of events and the number of clusters increase roughly exponentially with the cumulated snow load. The correlation coefficient is $R = 0.52$ for the number of events and $R = 0.60$ for the number of clusters. These correlations are significant at the 99% confidence level. There

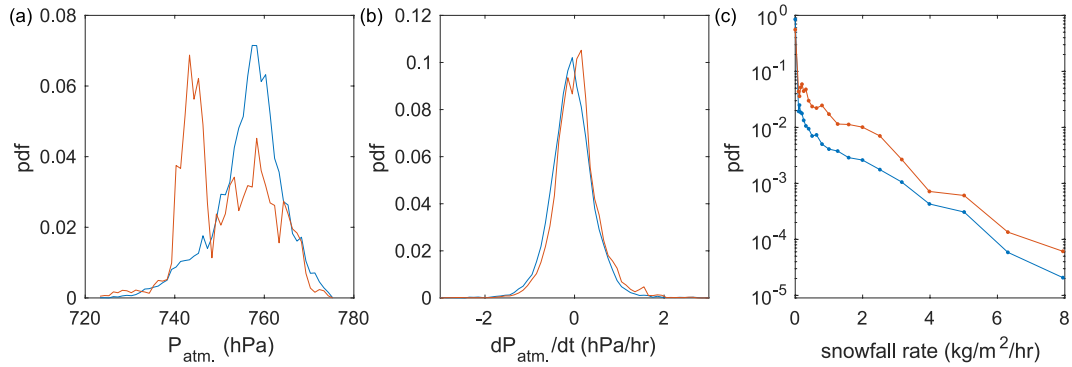

Figure 10. Probability distribution functions (pdfs) of the atmospheric pressure (a), hourly atmospheric pressure change (b), and snowfall rate (c). In each plot, the blue curve represents the pdf at all times during seismic acquisition, while the red curves shows the pdf at the times of low-frequency icequakes (LFIs). LFIs occur predominantly during low atmospheric pressure (a), increasing atmospheric pressure (b), and during snowfall episodes (c).

is however a considerable scatter around this trend, with many snowfall episodes not triggering repeaters. The magnitude of LFIs shows no significant correlation with the snow load.

4.4. Icequakes Location and Magnitudes

I selected all 96 clusters with at least seven phases picked by at least four stations, including at least one station outside Argentière Glacier. These criteria yield a horizontal location accuracy of about 1 km or less. A map is shown in Figure 1. Clusters are located all over the Mont-Blanc massif, from Glacier de Tré la Tête toward the South to Aiguille d'Argentière toward the North. Most clusters are located on or close to glaciers. For clusters outside glaciers, the distance to the closest glacier is generally smaller than the horizontal location accuracy. Figure 1 shows horizontal error ellipses corresponding to the 68% confidence interval, the length of theses ellipses should be multiplied by 1.62 to get the 95% confidence intervals.

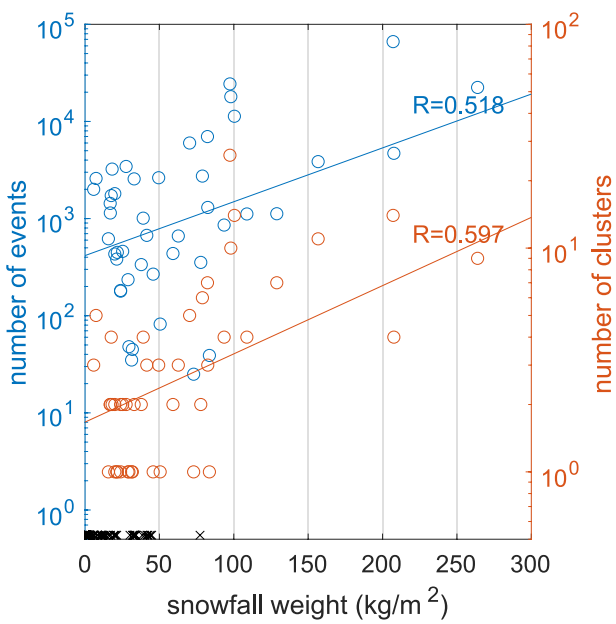

Figure 11. Evolution of the number of events (in blue) and of the number of activated clusters (in red) as a function of the snow load during each snowfall episode. Black crosses at the bottom indicate snowfall episodes that did not trigger any event.

Many clusters are located close to the crest between Aiguille des Grand Montets (near station N13) toward the West and Aiguille du Triolet toward the East. The high density of clusters in this area is likely a consequence of the distribution of seismic stations. Indeed, most seismic stations used for the detection (B01, B02, and B03) or the location (N13, N21, N3,1 and B04) are located on or close to Argentière glacier. Station BLANC was only used for the period 14 June 2019–1 June 2022 and is much noisier than stations B01, B02, and B03. Two clusters detected using station B03 as reference are located far away from Argentière Glacier, one cluster on the eastern face of Mont-Blanc and another cluster below the North face of Grandes Jorasses. The cluster located near the summit of Mont-Blanc has the largest magnitude and the best location accuracy. It was detected by 19 seismic stations up to 68 km away.

I also detected one cluster of LFIs located near Glacier de Trèlaporte (longitude 6.931°E and latitude 45.9054°N) and another below Glacier de l'Envers de Blaitière (6.928°E and 45.889°N) with unusual characteristics compared to the other clusters in the Mont-Blanc area. The cluster near Glacier de Trèlaporte is less regular than the other clusters and had a longer typical recurrence time (median of 33 min). Both clusters were located near 2,400 m a.s.l. about 100 m below the front of the glaciers and occurred mainly in late spring and summer. Given the location accuracy, they could possibly occur on the glaciers, which are likely temperate at this elevation. Or they could

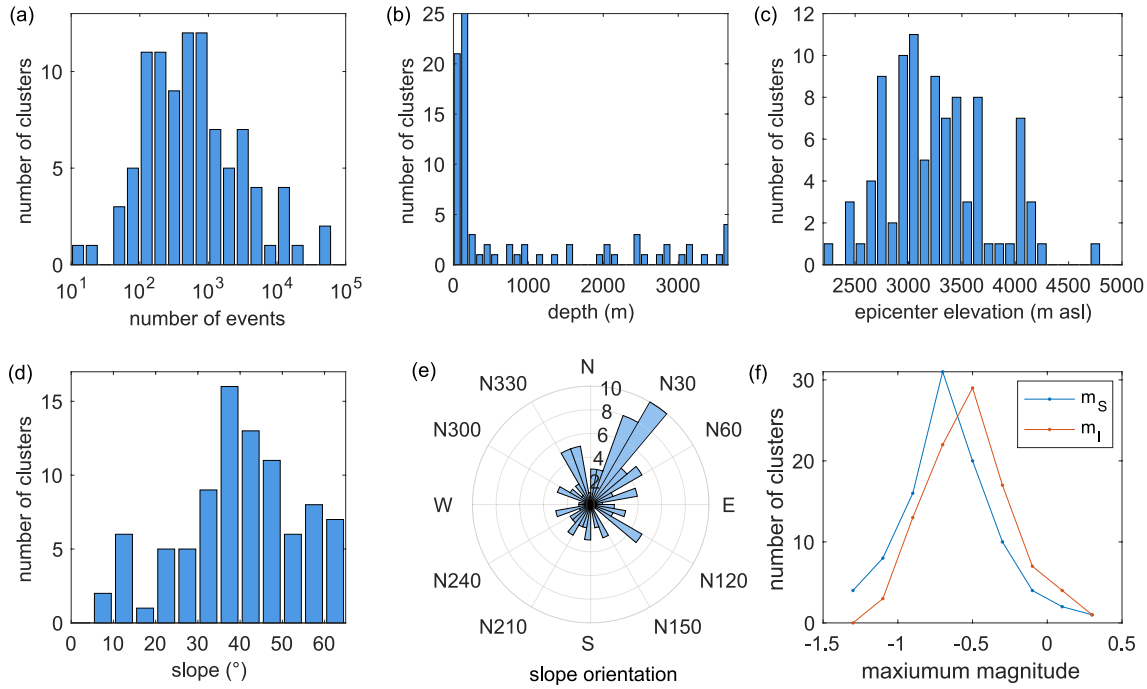

Figure 12. Characteristics of all located clusters: (a) distribution of the number of events per cluster (after removing temporally isolated events), (b) depth, (c) epicentral elevation, (d) slope and (e) slope orientation at the epicenter location, (f) surface wave and local magnitudes of the largest event of each cluster.

be associated with gravitational instabilities in the rock induced by the recent glacial retreat in this zone and promoted by the increase in meltwater in spring and summer.

Figure 12 illustrates the characteristics of all located clusters. Most events are shallower than 100 m. Estimated depths range between the surface and 3,664 m below, with an average of 746 m and a median of 107 m. Depth is generally smaller than vertical location error, with an average vertical error of 987 m (68% confidence interval). Icequake locations and depths are thus consistent with glacier basal sliding but the large vertical location error does not allow me to demonstrate this assumption and to exclude that LFIs could occur within the glacier. Epicenters are often above 3,000 m a.s.l, with an average value of 3,215 m. The average time residual is 0.14 s, comparable to values obtained for local earthquakes detected by Sismalp (https://sismalp.osug.fr) in the Mont-Blanc massif. This suggests that both the velocity model and the phase arrivals are correct. The local and surface magnitudes have very similar values ranging between −1.4 and 0.1. A linear fit gives $M_l = 0.85M_s + 0.02$ with a correlation coefficient of 0.93. The surface-waves magnitude M_s better explains the observed amplitudes, suggesting that seismic signals are dominated by surface waves. The average standard deviation of magnitudes between stations is 0.26 for M_s and 0.29 for M_l. The distribution of magnitudes is difficult to interpret due to the small number of clusters. The decay for $M < -1$ is likely due to the detection threshold and to the temporal changes in detection capacity when using different stations for detection.

Figure 13 shows the seismograms and spectra for the cluster located near the Mont-Blanc summit. The signal, stacked over all 446 events, is visible as far as 68 km away. The magnitude of the largest event is $M_S = 0$. The signal has the same frequency content over all stations with a peak near 5 Hz. This further suggests that this frequency peak is a source property and is not affected by attenuation.

4.5. Precursory Tremor-Like Signal

While most clusters start with small events and random occurrence times, one cluster initiated on 13 January 2021 as a large amplitude and long-duration signal. This cluster was located near Glacier de la Brenva (6.902°E and 45.836°N) with the epicenter at 3,250 m a.s.l. The signal during the first 1,000 s of this cluster is shown in Figure 14. The sequence started as a low-frequency but broadband signal (1–15 Hz) that lasted for about 100 s. It was detected at four seismic stations (BLANC, CI20, MFERR, and CI19). Because there is no visible P and S

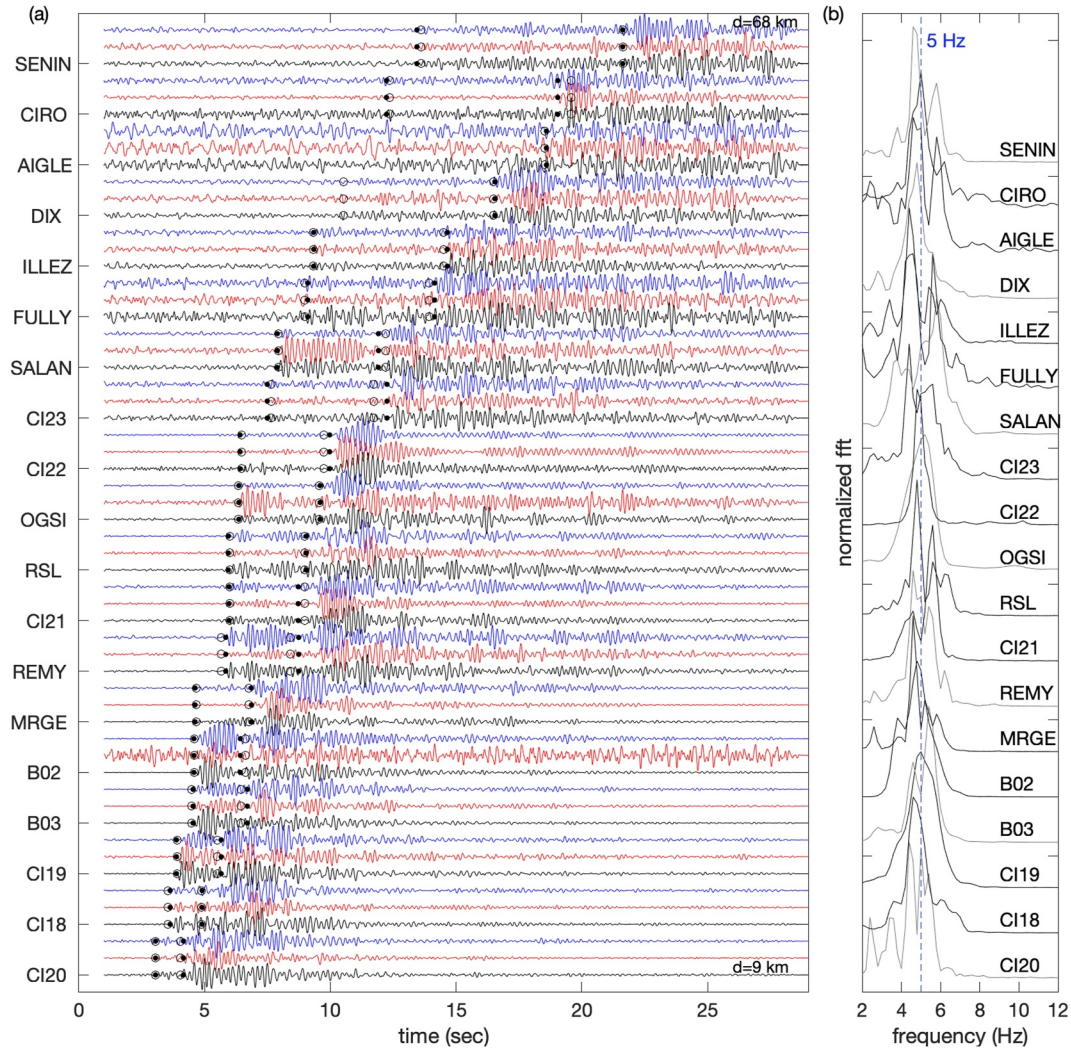

Figure 13. Seismograms (a and b) spectra at all stations where the icequake signal could be picked for the cluster located near the Mont-Blanc summit. Seismograms (ground velocity) were stacked over all events of the cluster, filtered between 2 and 20 Hz and normalized by the peak amplitude of each trace. Picks of P and S waves are shown as black dots and estimated arrival times as open circles. Stations are ordered according to their epicentral distance, from 9 km for station CI20 up to 68 km for station SENIN. Spectra of the vertical traces in panel (b) were also normalized by the peak value and shifted vertically for clarity.

waves, I could not locate this event accurately. Fixing the hypocenter at the location of the LFI cluster, the regional seismic network Sismalp (https://sismalp.osug.fr) provides an estimate of the magnitude $m_l = 0.1$. Two LFIs are detected at the beginning of this "tremor," with amplitudes larger than the following events. This suggests that this signal could be a swarm of overlapping LFIs, similar to non-volcanic tremor (Shelly et al., 2006, 2007). Winberry et al. (2013) also observed a tremor signal during slow-slip events at Whillans ice stream, with a much longer duration of 30 min, a broader spectral content and gliding spectral lines. Lipovsky and Dunham (2016) interpreted this tremor as a swarm of small repeating icequakes. But, in this study the "tremor" signal duration and frequency content is also similar to signals generated by snow avalanches, rockfalls or séracs falls. It could also be generated by water flow but this seems unlikely since it occurred in January above 3,000 m a.s.l.

4.6. Temporal Changes in Waveforms

Many clusters show progressive changes in waveforms, as illustrated in Figure 15 for the cluster with the largest number of events. This cluster located near the summit of Aiguille Verte was almost continuously active between

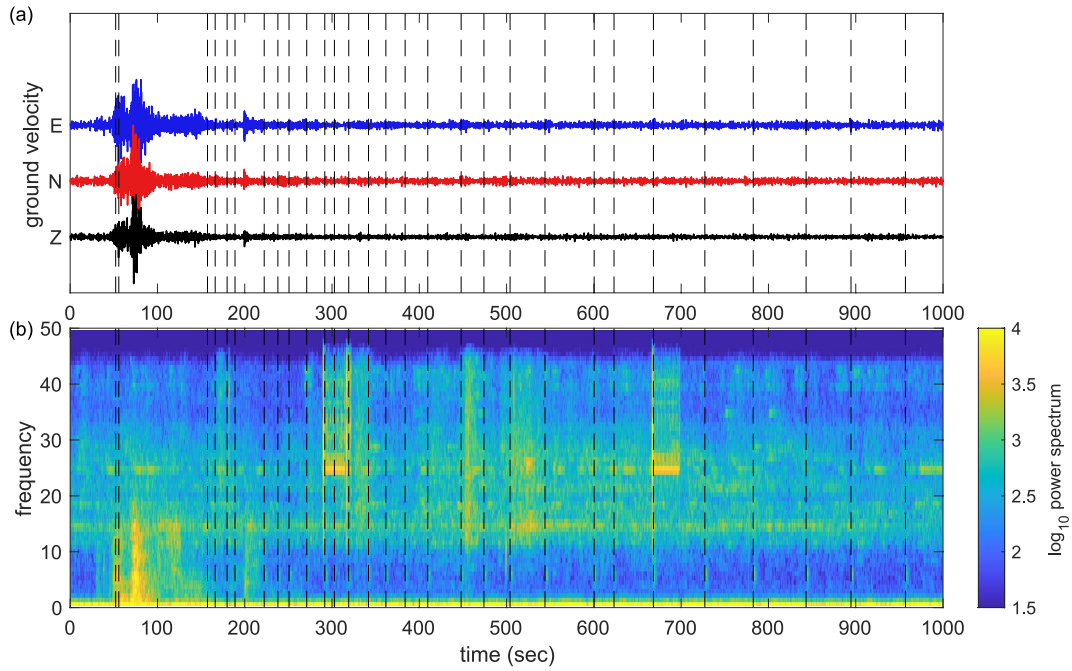

Figure 14. Seismograms (a and b) spectrogram of the signal recorded at station BLANC on 13 January 2021 at 21:55 UTC. Black vertical dashed lines correspond to low-frequency icequakes (LFIs). This cluster started at 21:55:52 and lasted for 15.78 hr. Seismograms in panel (a) are bandpass filtered between 1 and 10 Hz. A "tremor-like" signal is visible between about 50 and 150 s and contains two LFIs. Spectrogram in panel (b) is averaged over the three components.

11 December 2017 and 18 January 2018. During this period, I detected 28,978 events at station B01 located at 3.5 km from the source. This cluster is also shown in Figures 2–4. I applied a SVD-based Wiener filter to denoise the data (Moreau et al., 2017), keeping the first 15 singular values and the closest 3 neighbors in both time and event index. The first arrivals (P and S waves) show little variation with time, suggesting that the source did not migrate. Apparent variations of S-P arrival times could be due to uncertainties on P-wave picks. I see however clear progressive changes for late arrivals, as large as 0.3 s.

5. Discussion

5.1. Location and Basal Conditions

Most clusters are located on or near glaciers and at depths shallower than 100 m (Figure 12b). Icequake locations and depths are thus consistent with glacier basal sliding.I assume that LFIs are due to stick-slip events because other processes that generate icequakes, such as crevasse opening or icefalls, do not produce repeaters with quasi-periodic recurrence times, highly similar waveforms, and progressive changes in amplitudes and recurrence times (Allstadt & Malone, 2014; Helmstetter, Nicolas, et al., 2015; Röösli et al., 2016). Crevasse opening produces clusters of events with very different characteristics: wide amplitude distribution, temporal clustering, larger variability in waveforms (Helmstetter, Moreau, et al., 2015). I also assume that most LFIs are located at the ice-bed interface but the vertical location accuracy is too large to test this assumption. In previous studies, repeating icequakes or earthquakes have been located on major shear zones (ice-bed interface, major tectonic faults or subduction zones) (Podolskiy & Walter, 2016; Uchida & Bürgmann, 2019). Except on volcanoes, the stick-slip phenomenon is the only physical process that has been proposed to explain repeating events, therefore it seems unlikely that LFIs could be located within the glacier. Focal mechanisms could be used to estimate the source mechanism (e.g., fracture opening or slip, fault plane geometry and slip direction), but because LFI signals are monochromatic and emergent, it is non-trivial to identify the direction of P waves first arrivals. Basal icequakes lack surface waves when detected at short distance by sensors at the ice surface above the sources (e.g., Helmstetter, Nicolas, et al., 2015). In this study, sensors are located several kilometers away, which could explain the importance of surface waves.

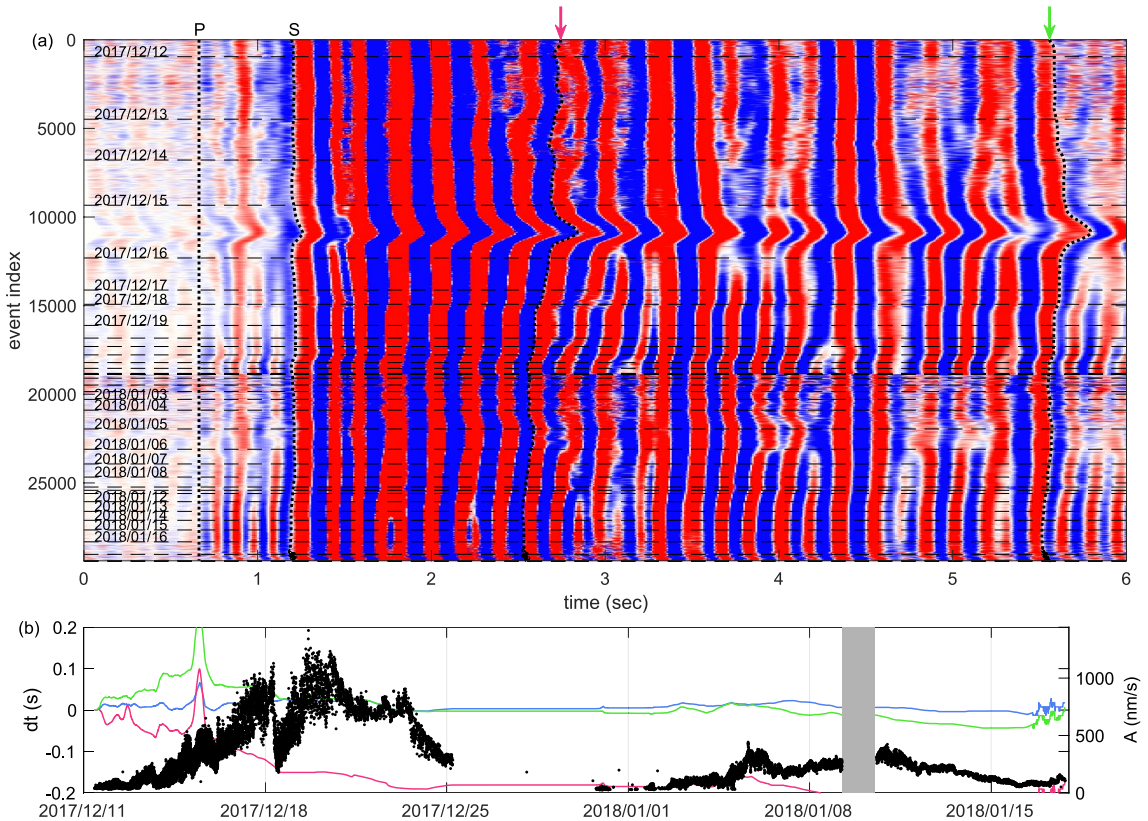

Figure 15. Temporal changes in waveforms for a cluster detected at station B01. (a) Seismogram for each event of the cluster. The color represents the ground velocity for the East component filtered between 2 and 20 Hz and normalized by the peak amplitude of each trace. I also applied a SVD-based Wiener filter (Moreau et al., 2017) to improve the signal-to-noise ratio. Seismograms are aligned on the P wave arrival time, which was picked on the vertical channel with a stronger P wave amplitude than the East component. The first two dotted lines correspond to P and S arrival times. The other two dotted lines marked by arrows correspond to late phase arrivals with strong temporal variations. Each dashed horizontal line corresponds to a new day. (b) Arrival time of different phases relative to the P wave arrival time and relative to the first event of the cluster: blue line for the S wave, pink and green lines for each phase indicated by a pink and green arrow respectively in panel (a). Black dots show the peak amplitude of each event. The gray area indicates a data gap.

Epicenters are often above 3,000 m a.s.l and mainly on steep and North facing slopes (Figures 1 and 12). At these locations, the presence of cold ice is possible. Indeed, a temperature of −2°C has been measured at the base of Tête Rousse glacier, at 3,100 m a.s.l. (Gilbert et al., 2012). Some clusters are clearly associated with cold-based ice, near Mont-Blanc summit or Col du Dôme. Vincent et al. (2020) measured a temperature of the ice close to the bedrock of −11°C at Col du Dôme at an elevation of 4,250 m a.s.l. Many clusters are located around 3,000 m a.s.l., possibly close to the transition between temperate and cold basal ice.

The basal ice temperature has a strong impact on glaciers dynamics. The motion of temperate glaciers (ice-bed interface at the melting point) is mainly due to basal slip, while cold-based hard-bedded glaciers (ice-bed interface below freezing) are thought to deform mainly by viscous flow in the bulk of the glacier (K. Cuffey & Paterson, 2010). There are however some observations of basal slip in polar glaciers at very cold temperatures (K. Cuffey & Paterson, 2010; K. M. Cuffey et al., 1999). The occurrence of LFIs on very steep slopes (Figure 12d) further suggests that these events occurred in cold based ice. Steep ice tends to remain in place because it is frozen to the bed (Faillettaz et al., 2015). Slope angle could be a better indicator for the presence of cold basal ice than elevation. When ice is frozen to the bed on steep slopes, ice motion occurs mainly through sérac falls and ice avalanches. Deformation by creep is limited due to the small thickness of steep cold-based glaciers. In this context, LFIs could be precursors of glacier collapse (Caplan-Auerbach & Huggel, 2007) or could indicate that basal ice is close to the melting point temperature. However, all LFIs analyzed in this study were not followed by any major glacier collapse.

Laboratory ice-on-rock or ice-on-till friction experiments have been used to infer how the frictional properties of ice depend on temperature. These experiments have shown a transition from a rate-weakening (friction

decreasing with sliding velocity) to a rate-strengthening behavior for increasing temperatures and a decrease of both healing and friction with temperature (McCarthy et al., 2017; Saltiel et al., 2021; Zoet et al., 2013). A rate-weakening behavior is required to generate dynamic rupture such as earthquakes or icequakes. The transition to rate-weakening friction is also favored by increasing sliding velocity, increasing debris concentration, and increasing drainage (McCarthy et al., 2017; Zoet et al., 2013). Other studies suggested that stick-slip events at the base of temperate glaciers or ice streams could be due to the friction of sediments entrained by the glacier motion (Lipovsky et al., 2019) or to the plowing of clasts embedded in the base of the ice through till (Barcheck et al., 2018; Thomason & Iverson, 2008). Basal drag on rough beds can also produce a rate-weakening behavior at large sliding velocities. Zoet and Iverson (2016) performed laboratory experiments with temperate ice sliding on a stepped bed and observed a decrease in basal drag with increasing sliding rate. However, the decrease in shear stress due to the growth of cavities occurs over several days. Therefore, this process may be too slow to generate stick-slip events with rupture duration of a few seconds and inter-event times of several minutes.

Two clusters are more likely associated with landslides below Glacier de Trélaporte and below Glacier de l'Envers de Blaitière. Repeating events have also been detected on landslides (e.g., Yamada et al., 2016). This suggests that there is not a single mechanism that explains all our observations, but that different physical processes may generate LFIs, likely different for temperate and cold-based glaciers. And that some of our "LFIs" may in fact be due to landslides.

Our observations are very similar to LFIs detected at Mount Rainier, an ice-covered volcano in the USA (Allstadt & Malone, 2014; Thelen et al., 2013). Both sites generate bursts of LFIs lasting for days or weeks and triggered by snowfall episodes. In both cases LFIs have similar properties: quasi-periodic recurrence times of a few minutes, magnitudes $-1 < M < 0$ and peak frequency around 5 Hz. Allstadt and Malone (2014) reported that Mount Rainier is a temperate glacier, whose displacement is dominated by basal sliding, and interpreted the LFIs at Mount Rainier as due to stick-slip on asperities surrounded by aseismic basal sliding. However, the location of icequakes at Mount Rainer is not well constrained, and they could be located near the top of the volcano (at 4,392 m a.s.l.) where the ice temperature is likely below the melting point (Mills, 1979).

Much larger and lower frequency icequakes repeat about twice a day at the base of Whillans Ice Stream in Antarctica because basal friction is modulated by oceanic tides (Bindschadler et al., 2003; Wiens et al., 2008). While most of the ice-stream is temperate at the base, the recent slowdown of the ice-stream and the occurrence of repeating stick-slip events may be due to basal freezing, with stick-slip events occurring on islands of cold based ice (Joughin et al., 2004; Saltiel et al., 2021).

5.2. Source Properties

From the magnitudes of LFIs, we can estimate possible values of source properties. The seismic moment M_o is related to the moment magnitude M_w by $M_w = \log_{10}(Mo)/1.5–6.03$ (Hanks & Kanamori, 1979). Assuming that our values of $-1.5 < M_s < 0.2$ are representative of M_w, I obtain a seismic moment ranging between 6.2×10^6 and 2.2×10^9 N.m for the largest event of each cluster. These values are much larger than the moment magnitude $-3.2 < M_w < -2.2$ estimated for the HFIs detected at Argentière glacier (Helmstetter, Nicolas, et al., 2015). The seismic moment is related to the shear modulus μ (2.3 GPa for ice), the slip d and the rupture area A by $M_0 = \mu A d$. I can thus only constrain the product of rupture area and slip. I can get a lower bound on the rupture radius $r = \sqrt{A/\pi}$ by assuming that during bursts of LFIs all the glacier displacement is due to seismic slip. This assumption may overestimate the seismic slip (and underestimate rupture length) if there is significant viscous deformation or underestimate d and over-estimate r if there is an acceleration of glacier displacement during bursts of LFIs. Cold glaciers move much slower than temperate glaciers. Vincent et al. (2020) measured a maximum ice flow velocity of 10 m/yr at Col du Dôme in 2017. The cluster located near the summit of Mont-Blanc has a magnitude $M_s = 0$ and a median recurrence time of 1,000 s. This gives a slip per event of 0.3 mm and a rupture length of 23 m. If only half of the displacement is due to basal slip, then the slip is 0.15 mm and the rupture length $r = 33$ m.

The stress drop $\Delta\tau$ can be estimated as

$$\Delta\tau = \mu \frac{d}{r} \frac{7\pi}{16} \quad (4)$$

for a circular rupture (Eshelby, 1957), yielding $\Delta\tau = 42$ kPa for $d = 0.3$ mm and a radius $r = 23$ m. This value is about one hundred times smaller than the value observed for tectonic earthquakes (Abercrombie, 1995). It is about 100 times larger than the normal stress induced by the smallest snowfall episode that trigger LFIs.

We can also estimate the rupture length from the main frequency of the signal, assuming that the peak in the spectrum corresponds to the corner frequency. Indeed, the lack of high frequency energy ($f > 10$ Hz) for the LFI signal shown in Figure 3 compared with a local earthquake and with a HFI suggests that the peak frequency of about 5 Hz could be a source property of LFIs.Allstadt and Malone (2014) observed similar low frequency signals at Mount Rainier and suggested that the lack of high-frequency waves was a path effect due to a low velocity zone created by the ice overlying a lower density, volcanic rubble and ejecta layer. This explanation cannot explain our observations in the Mont-Blanc area because there is no low velocity zone there; the bedrock is composed of granite or gneiss. Moreover, I observe the same spectral peak at all stations, both on or off of the ice (see Figure 13b), while Allstadt and Malone (2014) observed no clear shared spectral peaks between stations. This further suggests that this spectral peak near 5 Hz is a source property and is not affected by attenuation or site effects.

Madariaga (1976) derived the following relation between the rupture radius r and the corner frequency f_c

$$f_c = kV_S/r \tag{5}$$

for numerical 2D simulations of a circular crack expanding at a constant rupture velocity V_r. Assuming $V_r = 0.9V_S$, the constant k is equal to 0.21 for shear waves. Assuming $f_c = 5$ Hz and a shear wave velocity $V_S = 2{,}500$ m/s (intermediate between the value in the ice and in the bedrock) I obtain a source radius $r = 105$ m. This value is comparable with but larger than the length $r = 23$ m estimated above from the maximum seismic moment and the glacier velocity. This suggests that LFIs only account for a small fraction of glacier displacement rate even during bursts of LFIs. Using this value of the source radius $r = 105$ m and a magnitude $M_w = 0$, I obtain a slip of 14 μm and a stress drop of 0.4 kPa comparable with the stress change induced by snowfalls.

5.3. Temporal Changes in Waveforms

Many clusters of repeating LFIs show progressive changes in waveforms, as illustrated in Figure 15. Figure 15a shows the waveforms of a cluster of 28,000 LFIs that occurred near the summit of Aiguille Verte about 3.5 km south of station B01. Arrival times in the coda of both P and S waves vary by up to 0.2 s while the first arrivals show smaller changes that could be due to picking errors (Figure 15b). This suggests that the nucleation point does not evolve during clusters, that is, there is no evidence for migration in time. Based on a single station, we cannot exclude a migration of the order of tens or even hundreds of meters. But, the large change in arrival times on 15 December 2017 is transient and goes back to its initial value after a few hours. It is hard to understand how a source could migrate with the glacier first upstream and then downstream.

Changes in waveforms can be due to changes in the medium or to changes in source properties, either rupture area or rupture velocity. However, such rapid (a few hours or days) and large changes in travel times (up to 10%) are unlikely to result from changes in the medium. Guillemot et al. (2020) reported changes in seismic wave velocity in a permafrost zone but these changes were much smaller (about 1%) and slower.Indeed, most LFI clusters occur in winter at large elevations where there is no or very little water. The snow layer evolves with time but the low-frequency seismic waves near 5 Hz are not strongly sensitive to this shallow layer. I thus propose two explanations for these changes in seismic signals, either changes in the rupture area or changes in the rupture velocity. Both parameters control the rupture duration and the signal frequency content. Allstadt and Malone (2014) also observed a progressive change in waveforms within each cluster using coda wave interferometry, which they interpreted as due to a migration of the source with the glacier flow.

A very slow rupture velocity of about 88 m/s has been measured for repeating basal icequakes at Whillans Ice Stream in West Antarctica (Bindschadler et al., 2003). But, this rupture velocity is similar to the shear wave velocity in the till layer where rupture propagates. Walter et al. (2011) further observed temporal changes in rupture velocity between 100 and 300 m/s between successive events, correlated with inter-event times and slip amount. Walter et al. (2015) reproduced these results in a laboratory stick-slip experiment, showing that rupture velocity depends on pre-rupture stress. A progressive change in rupture velocity could explain our observations of changes in seismic waveforms. However, I found no clear correlation between changes in seismic waveform and changes

in the amplitude of repeating LFIs (see Figure 15b). I thus don't know how to explain these possible changes in rupture velocity or rupture length.

It is not clear whether the long signal duration is due to the source or to the seismic waves propagation. If the rupture lasts for several seconds, it suggests a very slow rupture to be consistent with the rupture size $r = 105$ m estimated from Equation 5. Because of the shallow source, of the heterogeneous medium and of the complex topography, it is possible that the late arrivals are diffracted or reflected waves rather than direct waves. Numerical simulations of the rupture in a complex medium could help to understand this change in waveforms.

5.4. Correlation With Snowfall Episodes

Repeating LFIs are mainly observed during and after snowfall episodes, while HFIs are not sensitive to snowfalls (Helmstetter, Nicolas, et al., 2015). There is however, a large variability in the number of LFIs for the same snow load (Figure 11). This variability could be partly explained by the effect of snow redistribution by avalanches and wind. Snow redistribution can alter by more than an order of magnitude how much snow is deposited in a small location Both avalanches and wind tend to decrease the snow load on steep slopes where most LFIs occur, which could explain the progressive decrease in amplitude and recurrence times during bursts of LFIs. At places where snow accumulates after a snowfall episode, snow transfer could explain the time delay between the peak of snowfall rate and the peak of the LFIs rate. It could also explain the large number of LFIs triggered by some small snowfall episodes.

Allstadt and Malone (2014) suggested that additional loading due to snowfalls perturbs the glaciers from smooth sliding to stick-slip regime. Using a rate-and-state friction law (Dieterich, 1979) to model the sliding of the glacier over its bed, we can indeed reproduce a transition from stable sliding to the stick-slip regime by increasing normal stress (Helmstetter et al., 2018; Lipovsky & Dunham, 2017). The increase in normal stress associated with snowfalls is however partly canceled by the associated decrease in atmospheric pressure, but the overall effect of atmospheric pressure and snow load tends to increase the normal stress toward the end of each snowfall episode, when most LFIs occur (Figure 9). However, the average rate of LFIs starts to increase when the total load (snow and atmospheric pressure) increases but is still negative. This suggests that the rate of LFIs correlates more with the stress rate than with the stress. In the context of rate-and-state friction, seismicity rate correlates with stress for short-period oscillating stresses and with stress rate for slow stress perturbations compared with the nucleation time (Heimisson & Avouac, 2020). Based on this model, the correlation between the rate of LFIs and pressure rate suggests that the nucleation time of LFIs is much smaller than 1 day.

The change in normal stress associated with snowfalls is very small compared with the normal stress at the base of glaciers. A snowfall of 25 cm with a density of 200 kg/m^3 increases the normal stress by about 5 hPa, about 0.05% of the normal stress at the base of a 100 m thick glacier. It is thus surprising that such a small stress change triggers so many LFIs. However, earthquakes have been shown to be sensitive to even smaller relative stress perturbations. Seismicity is modulated by ocean tides, corresponding to a stress change of about 10 kPa, while the normal stress at 10 km depth is about 300 MPa (Thomas et al., 2009). This high susceptibility of earthquakes and LFIs suggests that faults and ice-bed interfaces are very close to the rupture threshold, at least at some points, and that rupture initiates rapidly when stress reaches the failure threshold. Allstadt and Malone (2014) suggested that the direct loading by snowfalls could be amplified and delayed by changes in subglacial hydrology. This process is however not relevant for cold based glaciers.

For Alpine glaciers very close to the melting point temperature, another mechanism could explain the triggering by snowfalls. The additional weight induced by snowfalls slightly decreases the melting point temperature, so that the basal temperature may reach the melting point temperature. The increase in pressure due to a snowfall of 50 cm with a density of 200 kg/m^3 is about 1 kPa, leading to a change in melting temperature of about 10^{-4}°C (Clausius-Clapeyron constant). For subfreezing temperatures, Shreve (1984) and Fowler (1986) suggested that there is a significant amount of basal slip, with a sliding velocity increasing very rapidly as temperature gets closer to the melting point temperature. Therefore, this mechanism may only be active very close to the transition between cold-based and temperate glaciers. Snowfall episodes are also associated with an average drop of air temperature of about 4°C. Assuming heat transfer in the ice by conduction with a thermal diffusivity k of 1.1×10^{-6} m^2/s, the change in temperature at depth is very small (about 0.001°C at a depth of 10 m). Moreover,

the temperature propagates very slowly at depth with a typical diffusion time $\approx z^2/k$, about 1,000 days at a depth z of 10 m. Therefore the change in temperature at depth cannot explain the triggering of LFIs by snowfalls.

The correlation between snowfalls and LFIs could suggest that LFIs occur within or at the base of the fresh snow layer due to snow avalanches, snow settling or fracture propagation. But then, it is difficult to explain why LFIs occur regularly in time and why they mainly occur above 3,000 m a.s.l. And because seismic waves attenuate very fast in the snow and the shear modulus is much smaller in the snow than in the ice, it is difficult to explain how the signal could be detected up to 68 km away.

Repeating LFIs triggered by snowfalls have also been detected on Gugla rock glacier in Switzerland (Guillemot et al., 2020; Helmstetter et al., 2018). These studies suggested that these events were associated with stick-slip behavior at the base of the rock-glacier. However, I realized that most clusters detected at Gugla were also visible at other permanent seismic stations (stations MMK, SIMPL, EMBD, SNIB, VANNI, and DIX in Switzerland, network code CH and Italian station SATI, network code GU). Several clusters have been located at distances between 2 and 7 km East or South-East from Gugla. These locations are not very accurate but are all possibly associated with glaciers above 3,000 m a.s.l. These events are thus very similar to LFIs in the Mont-Blanc area and may be produced by the same physical processes.

5.5. Comparison With Earthquakes

Both faults and subglacial slip exhibit a wide spectrum of behavior, from stable slow slip to dynamic rupture, with transient slip events ranging over a wide range of spatial and temporal scales (Peng & Gomberg, 2010). Tectonic faults and subduction zones produce both fast earthquakes, with rupture duration of the order of seconds, and slow slip events, with duration of days or months, and probably a continuum of slip modes in between (Thøgersen et al., 2019). LFIs in the Mont-Blanc area share several properties with low-frequency earthquakes (LFEs). LFEs are due to shear slip on faults like regular earthquakes but their signal lacks high frequency energy. They are mainly detected on transform faults (e.g., San Andreas) or subduction zones in the lower part of the locked seismogenic zone near the brittle-ductile transition (Shelly et al., 2006, 2007). LFEs have much smaller stress drops, smaller slip-rates and smaller rupture velocities than regular earthquakes (Thomas et al., 2016). Like LFIs, LFEs can be triggered by very small perturbations, like distant earthquakes or tides. Thomas et al. (2009) observed that LFEs on the San Andreas are very sensitive to tidally induced shear stress changes with peak-to-peak amplitudes less than 0.5 kPa.

Both LFEs and LFIs seem to occur mainly on spots on faults or glacier beds near the transition between stable sliding (for temperate basal ice for LFIs and below the seismogenic zone for LFEs) and locked areas (for cold basal ice for LFIs and in the seismogenic zone for LFEs). LFEs are more sensitive than regular earthquakes to small stress changes. Similarly, the snowfalls that trigger LFIs in the Mont-Blanc area do not produce any increase in the rate of HFIs (Helmstetter, Nicolas, et al., 2015).

Repeating earthquakes occur regularly on the same asperity. The quasi-periodic behavior of repeaters is commonly explained by a constant aseismic sliding rate around the asperity (Nadeau et al., 1995; Uchida & Bürgmann, 2019). Aseismic slip increases the stress on the asperity between events. Rupture occurs when the stress reaches a threshold. Stress decreases during rupture and increases again until the next event. This mechanism can also explain the repeating HFIs on temperate glaciers, which have a large amount of aseismic basal slip. However, many LFIs occur on cold-based glaciers, so that there is very little slip at the ice-bed interface. The reloading between stick-slip events may thus be due to viscous creep within the bulk of the glacier rather than from slip around the asperity.

6. Conclusion and Perspectives

I discovered repeating LFIs in the Mont-Blanc massif. Some clusters of LFIs are located on cold based glaciers (e.g., near Mont-Blanc summit or near Col du Dôme), a few ones on temperate glaciers or possibly on rockslides activated by glacial unloading. For most clusters the basal conditions are unknown but are likely close to the melting point temperature.

I found both similarities and major differences between repeating HFIs and LFIs. Both LFIs and HFIs occur more or less regularly in time, repeating every few minutes, and display progressive changes in amplitude and

recurrence times. While HFIs are located at the base of temperate alpine glaciers, most LFIs are located at higher elevations where cold-based ice is expected. LFIs are triggered by snowfalls while HFIs are not sensitive to snowfalls.

The source properties (depth, rupture length, rupture velocity, and stress drop) of LFIs are difficult to estimate because I do not have near-field data. LFIs are difficult to monitor because they occur mainly at high elevations, on steep faces exposed to snow avalanches or serac falls. Installing seismometers in such places is thus difficult and dangerous. In addition, bursts of LFIs usually last for a few days and mainly occur during snowfall episodes. Even if we can detect and locate in real time the beginning of a cluster, we cannot go in the field to install seismometers nearby when the weather is bad, and LFIs often stop before the weather improves. Satellite images could be used remotely and retrospectively to estimate glacier motion. They could be used to test whether the glacier accelerates during bursts of LFIs or if bursts of LFIs occur at constant displacement rate. LFIs could be due to a transition between creep-dominated deformation within the glacier and basal stick-slip motion. However, while some studies have estimated the average displacement rate in the Mont-Blanc area, the resolution is not yet good enough to detect short-term (days to weeks) temporary variations in velocity (Millan et al., 2019).

Similar repeating LFIs have also been observed in the Swiss Alps (Helmstetter et al., 2018) and at Mount Rainier (Allstadt & Malone, 2014). They probably occur elsewhere on Alpine glaciers. Trying to detect these events using existing regional seismic networks near glaciated areas could help us to understand the link between LFIs and glacier basal conditions.

Numerical modeling could be interesting to learn more about LFIs source processes and triggering mechanisms. We could try to simulate seismic signals of LFIs by changing the rupture velocity or the rupture length to reproduce the observed temporal changes in seismic waveforms. Several processes could explain the triggering of LFIs by snowfalls, either due to the increase in normal and shear stress or due the tiny change in melting point temperature with pressure. Numerical simulations could be used to test both hypotheses. Helmstetter et al. (2018) already attempted to reproduce repeating LFIs using the rate-and-state friction law. However, they assumed aseismic basal slip around the asperity. Our observations suggest that most LFIs occur on cold-based glaciers, so that deformation is dominated by viscous creep rather than by basal slip. We could also test different friction laws developed for basal sliding, such as the model of Gagliardini et al. (2007).

The differences between HFIs and LFIs are similar to the ones between regular earthquakes and LFEs, suggesting that they reflect common physical processes controlling rupture nucleation and propagation. Low-frequency events are more sensitive to smaller perturbations, occur near the transition between the locked and the creeping areas, and have slower rupture velocities and smaller stress drop compared with high-frequency events. Understanding what controls the nucleation of LFIs could yield important information on basal properties and their temporal evolution.

Data Availability Statement

Some seismological data are available from the Federation of Digital Seismograph Networks (FDSN) with network codes CH, GU, IV, FR, ZO, 1D, and 8C. FDSN data centers are available from https://www.fdsn.org/networks. The list of all seismic stations used and network codes are given in Table 1. Some data are distributed by FDSN with restricted access (network codes XT, 8D). Data from temporary stations B01-B04, DOM, and MDG on glaciers in the massif are not (yet) open. Catalogs of repeating LFIs and cluster locations are provided at https://doi.org/10.5281/zenodo.6822165. Meteorological data are available from GLACIOCLIM observatory (https://glacioclim.osug.fr) and S2M database (Vernay et al., 2019). We used nonlinloc software (Lomax et al., 2000) to locate LFIs. This program can be downloaded from http://alomax.free.fr/nlloc/ and my input files (station locations, arrival times, velocity models, and topography) can be downloaded from https://doi.org/10.5281/zenodo.6822165. Sismalp earthquake catalog is available from ist-sc3-geobs.osug.fr:8080 using FDSN web services.

Acknowledgments
The author thank Florent Gimbert and Ugo Nanni for sharing their seismic data (stations B01-B04, DOM, and MDG) and Toni Kraft for providing data of stations MFERR, VFER2, and AMID2. The author thank Benoit Urruty, Laurent Ott, and others for their help in the field. Some instruments (nodes N11-N35, new stations CI18-CI20) belong to the French National Pool of Portable Seismic Instruments (Sismob-RESIF). Sismob is member of the French seismological and geodetic network Resif-Epos, a Research Infrastructure (RI) managed by CNRS-Insu. The author thank Michel Bouchon, Florent Gimbert, Ugo Nanni, James Hollingsworth, Emmanuel Chaljub, Mathieu Causse, Luc Moreau, and Roland Bürgmann for interesting discussions. Chris Carr, Yoram Terleth, and two anonymous reviewers provided very insightful comments that helped to improve the manuscript. This work was supported by the SAUSSURE project (https://saussure.osug.fr) (ANR-18-CE01-0015) funded by the Agence National de la Recherche (ANR). This work was also partially funded by the SISM@LP-Swarm project (POIA-FEDER Grant, funded by the European Commission FEDER, Région SUD and Agence Nationale de la Cohésion des Territoires). ISTerre is part of Labex OSUG@2020 (ANR10 LABX56).

References

Abercrombie, R. E. (1995). Earthquake source scaling relationships from -1 to 5 M_L using seismograms recorded at 2.5-km depth. *Journal of Geophysical Research*, *100*(B12), 24015–24036. https://doi.org/10.1029/95jb02397

Allen, R. V. (1978). Automatic earthquake recognition and timing from single traces. *Bulletin of the Seismological Society of America*, *68*(5), 1521–1532. https://doi.org/10.1785/bssa0680051521

Allstadt, K., & Malone, S. D. (2014). Swarms of repeating stick-slip icequakes triggered by snow loading at Mount Rainier volcano. *Journal of Geophysical Research: Earth Surface*, *119*(5), 1180–1203. https://doi.org/10.1002/2014JF003086

Barcheck, C. G., Tulaczyk, S., Schwartz, S. Y., Walter, J. I., & Winberry, J. P. (2018). Implications of basal micro-earthquakes and tremor for ice stream mechanics: Stick-slip basal sliding and till erosion. *Earth and Planetary Science Letters*, *486*, 54–60. https://doi.org/10.1016/j.epsl.2017.12.046

Bindschadler, R. A., Vornberger, P. L., King, M. A., & Padman, L. (2003). Tidally driven stick-slip motion in the mouth of Whillans Ice Stream, Antarctica. *Annals of Glaciology*, *36*, 263–272. https://doi.org/10.3189/172756403781816284

Bormann, P., & Dewey, J. W. (2014). The new IASPEI standards for determining magnitudes from digital data and their relation to classical magnitudes. In P. Bormann (Ed.), *New Manual of Seismological Observatory Practice 2 (NMSOP-2), Potsdam: Deutsches GeoForschungsZentrum GFZ* (pp. 1–44). https://doi.org/10.2312/GFZ.NMSOP-2_IS_3.3

Caplan-Auerbach, J., & Huggel, C. (2007). Precursory seismicity associated with frequent, large ice avalanches on Iliamna Volcano, Alaska, USA. *Journal of Glaciology*, *53*(180), 128–140. https://doi.org/10.3189/172756507781833866

Cuffey, K., & Paterson, W. (2010). *The physics of glaciers*. Elsevier, Butterworth-Heinemann.

Cuffey, K. M., Conway, H., Hallet, B., Gades, A. M., & Raymond, C. F. (1999). Interfacial water in polar glaciers, and glacier sliding at −17°C. *Geophysical Research Letters*, *26*(6), 751–754. https://doi.org/10.1029/1999GL900096

Dieterich, J. H. (1979). Modeling of rock friction, 1. Experimental results and constitutive equations. *Journal of Geophysical Research*, *84*(B5), 2169–2175. https://doi.org/10.1029/JB084iB05p02169

Echelmeyer, K., & Zhongxiang, W. (1987). Direct observations of basal sliding and deformation of basal drift at sub-freezing temperatures. *Journal of Glaciology*, *33*(113), 83–98. https://doi.org/10.3189/s0022143000005396

Eshelby, J. D. (1957). The determination of the elastic field of an ellipsoidal inclusion, and related problems. *Proceedings of the royal society of London. Series A. Mathematical and physical sciences*, *241*(1226), 376–396. https://doi.org/10.1098/rspa.1957.0133

Faillettaz, J., Funk, M., & Vincent, C. (2015). Avalanching glacier instabilities: Review on processes and early warning perspectives. *Review of Geophysics*, *53*(2), 203–224. https://doi.org/10.1002/2014RG000466

Fowler, A. C. (1986). Sub-temperate basal sliding. *Journal of Glaciology*, *32*(110), 3–5. https://doi.org/10.1017/S0022143000006808

Gagliardini, O., Cohen, D., Råback, P., & Zwinger, T. (2007). Finite-element modeling of subglacial cavities and related friction law. *Journal of Geophysical Research*, *112*(F2), F02027. https://doi.org/10.1029/2006JF000576

Gibbons, S. J., & Ringdal, F. (2006). The detection of low magnitude seismic events using array-based waveform correlation. *Geophysical Journal International*, *165*(1), 149–166. https://doi.org/10.1111/j.1365-246x.2006.02865.x

Gilbert, A., Vincent, C., Wagnon, P., Thibert, E., & Rabatel, A. (2012). The influence of snow cover thickness on the thermal regime of Tête Rousse Glacier (Mont Blanc range, 3200 m a.s.l.): Consequences for outburst flood hazards and glacier response to climate change. *Journal of Geophysical Research*, *117*(F4), F04018. https://doi.org/10.1029/2011JF002258

Gimbert, F., Nanni, U., Roux, P., Helmstetter, A., Garambois, S., Lecointre, A., et al. (2021). A multi-physics experiment with a temporary dense seismic array on the Argentière Glacier, French Alps: The RESOLVE project. *Seismological Research Letters*, *92*(2A), 1185–1201. https://doi.org/10.1785/0220200280

Guillemot, A., Helmstetter, A., Larose, E., Baillet, L., Garambois, S., Mayoraz, R., & Delaloye, R. (2020). Seismic monitoring in the Gugla rock glacier (Switzerland): Ambient noise correlation, microseismicity and modelling. *Geophysical Journal International*, *221*(3), 1719–1735. https://doi.org/10.1093/gji/ggaa097

Hanks, T. C., & Kanamori, H. (1979). Moment magnitude scale. *Journal of Geophysical Research*, *84*(B5), 2348–2350. https://doi.org/10.1029/jb084ib05p02348

Heimisson, E. R., & Avouac, J. P. (2020). Analytical prediction of seismicity rate due to tides and other oscillating stresses. *Geophysical Research Letters*, *47*(23), e2020GL090827. https://doi.org/10.1029/2020GL090827

Helmstetter, A., Guéguen, P., & RESIF. (2020). Seismic network 8C: Monitoring swarms in the Mont-Blanc and Vallorcine area (RESIF – SISMOB) [Dataset]. RESIF – Réseau Sismologique et géodésique Français. https://doi.org/10.15778/RESIF.8C2019

Helmstetter, A., Lipovsky, B., Larose, E., Baillet, L., & Mayoraz, R. (2018). Repeating quakes triggered by snow-falls at Gugla rock-glacier: Transition between stable slip and stick-slip? *Annual Meeting of the Seismological Society of America, Seismological. Research Letter*, *89*(2B), 824.

Helmstetter, A., Moreau, L., Nicolas, B., Comon, P., & Gay, M. (2015). Intermediate-depth icequakes and harmonic tremor in an Alpine glacier (Glacier d'Argentière, France): Evidence for hydraulic fracturing? *Journal of Geophysical Research: Earth Surface*, *120*(3), 402–416. https://doi.org/10.1002/2014JF003289

Helmstetter, A., Nicolas, B., Comon, P., & Gay, M. (2015). Basal icequakes recorded beneath an alpine glacier (Glacier d'Argentière, Mont Blanc, France): Evidence for stick-slip motion? *Journal of Geophysical Research: Earth Surface*, *120*(3), 379–401. https://doi.org/10.1002/2014JF003288

Helmstetter, A., & RESIF. (2020). Seismic network 1D: Temporary installation of 13 sensors (3C fairfield nodes) on Argentière Glacier and near Col des Grands Motets in the Mont Blanc massif (RESIF-SISMOB) [Dataset]. RESIF – Réseau Sismologique et géodésique Français. https://doi.org/10.15778/RESIF.1D2019

INGV Seismological Data Centre. (2006). Rete Sismica Nazionale (RSN), Istituto Nazionale di Geofisica e Vulcanologia (INGV), Italy [Dataset]. https://doi.org/10.13127/SD/X0FXnH7QfY

Jarvis, A., Guevara, E., Reuter, H. I., & Nelson, A. D. (2008). Hole-filled SRTM for the globe: Version 4: Data grid. Web publication/site, CGIAR Consortium for Spatial Information. Retrieved from http://srtm.csi.cgiar.org/

Joughin, I., Tulaczyk, S., MacAyeal, D. R., & Engelhardt, H. (2004). Melting and freezing beneath the Ross ice streams, Antarctica. *Journal of Glaciology*, *50*(168), 96–108. https://doi.org/10.3189/172756504781830295

Kufner, S. K., Brisbourne, A. M., Smith, A. M., Hudson, H. S., Murray, T., Schlegel, R., et al. (2021). Not all icequakes are created equal: Basal icequakes suggest diverse bed deformation mechanisms at Rutford Ice Stream, West Antarctica. *Journal of Geophysical Research: Earth Surface*, *126*(3), e2020JF006001. https://doi.org/10.1029/2020JF006001

Lipovsky, B. P., & Dunham, E. M. (2016). Tremor during ice-stream stick slip. *The Cryosphere*, *10*(1), 385–399. https://doi.org/10.5194/tc-10-385-2016

Lipovsky, B. P., & Dunham, E. M. (2017). Slow-slip events on the Whillans Ice Plain, Antarctica, described using rate-and-state friction as an ice stream sliding law. *Journal of Geophysical Research: Earth Surface*, *122*(4), 973–1003. https://doi.org/10.1002/2016JF004183

Lipovsky, B. P., Meyer, C. R., Zoet, L. K., McCarthy, C., Hansen, D. D., Rempel, A. W., & Gimbert, F. (2019). Glacier sliding, seismicity and sediment entrainment. *Annals of Glaciology*, *60*(79), 182–192. https://doi.org/10.1017/aog.2019.24

Lomax, A., Virieux, J., Volant, P., & Berge, C. (2000). Probabilistic earthquake location in 3D and layered models: Introduction of a Metropolis-Gibbs method and comparison with linear locations. In C. H. Thurber & N. Rabinowitz (Eds.), *Advances in seismic event location Thurber* (pp. 101–134). Kluwer.

Madariaga, R. (1976). Dynamics of an expanding circular fault. *Bulletin of the Seismological Society of America*, *66*(3), 639–666. https://doi.org/10.1785/bssa0660030639

McCarthy, C., Savage, H., & Nettles, M. (2017). Temperature dependence of ice-on-rock friction at realistic glacier conditions. *Philosophical Transactions of the Royal Society A: Mathematical, Physical and Engineering Sciences*, *375*(2086), 20150348. https://doi.org/10.1098/rsta.2015.0348

Millan, R., Mouginot, J., Rabatel, A., Jeong, S., Cusicanqui, D., Derkacheva, A., & Chekki, M. (2019). Mapping surface flow velocity of glaciers at regional scale using a multiple sensors approach. *Remote Sensing*, *11*(21), 2498. https://doi.org/10.3390/rs11212498

Mills, H. H. (1979). Some implications of sediment studies for glacial erosion on Mount Rainier, Washington. *Northwest Science*, *53*(3), 190–199.

Moreau, L., Stehly, L., Boué, P., Lu, Y., Larose, E., & Campillo, M. (2017). Improving ambient noise correlation functions with an SVD-based Wiener filter. *Geophysical Journal International*, *211*(1), 418–426. https://doi.org/10.1093/gji/ggx306

Nadeau, R. M., Foxall, W., & McEvilly, T. V. (1995). Clustering and periodic recurrence of microearthquakes on the San Andreas fault at Parkfield, Calif. *Science*, *267*(5197), 503–507. https://doi.org/10.1126/science.267.5197.503

Nanni, U., Gimbert, F., Vincent, C., Gräff, D., Walter, F., Piard, L., & Moreau, L. (2020). Seasonal and diurnal dynamics of subglacial channels: Observations beneath an Alpine Glacier. *The Cryosphere*, *14*(5), 1475–1496. https://doi.org/10.5194/tc-14-1475-2020

Peng, Z., & Gomberg, J. (2010). An integrated perspective of the continuum between earthquakes and slow-slip phenomena. *Nature Geoscience*, *3*(9), 599–607. https://doi.org/10.1038/ngeo940

Podolskiy, E. A., & Walter, F. (2016). Cryoseismology. *Review of Geophysics*, *54*(4), 2016RG000526. https://doi.org/10.1002/2016RG000526

RESIF. (1995). RESIF-RLBP French Broad-band network, RESIF-RAP strong motion network and other seismic stations in metropolitan France [Dataset]. RESIF – Réseau Sismologique et géodésique Français. https://doi.org/10.15778/RESIF.FR

Röösli, C., Helmstetter, A., Walter, F., & Kissling, E. (2016). Meltwater influences on deep stick-slip icequakes near the base of the Greenland Ice Sheet. *Journal of Geophysical Research: Earth Surface*, *121*(2), 2015JF003601. https://doi.org/10.1002/2015JF003601

Roux, P., Gimbert, F., & RESIF. (2021). Dense nodal seismic array temporary experiment on Alpine Glacier of Argentière (RESIF-SISMOB) [Dataset]. RESIF – Réseau Sismologique et géodésique Français. https://doi.org/10.15778/RESIF.ZO2018

Saltiel, S., McCarthy, C., Creyts, T. T., & Savage, H. M. (2021). Experimental evidence of velocity-weakening friction during ice slip over frozen till: Implications for basal seismicity in fast moving, soft-bed glaciers and ice streams. *Seismological Research Letters*, *92*(5), 2793–2810. https://doi.org/10.1785/0220200480

Schaff, D. P., & Richards, P. G. (2011). On finding and using repeating seismic events in and near China. *Journal of Geophysical Research*, *116*(B3), B03309. https://doi.org/10.1029/2010JB007895

Shelly, D. R., Beroza, G. C., & Ide, S. (2007). Non-volcanic tremor and low-frequency earthquake swarms. *Nature*, *446*(7133), 305–307. https://doi.org/10.1038/nature05666

Shelly, D. R., Beroza, G. C., Ide, S., & Nakamula, S. (2006). Low-frequency earthquakes in Shikoku, Japan, and their relationship to episodic tremor and slip. *Nature*, *442*(7099), 188–191. https://doi.org/10.1038/nature04931

Shreve, R. L. (1984). Glacier sliding at subfreezing temperatures. *Journal of Glaciology*, *30*(106), 341–347. https://doi.org/10.3189/s0022143000006195

Six, D., & Vincent, C. (2014). Sensitivity of mass balance and equilibrium-line altitude to climate change in the French Alps. *Journal of Glaciology*, *60*(223), 867–878. https://doi.org/10.3189/2014JoG14J014

Smith, A. M. (2006). Microearthquakes and subglacial conditions. *Geophysical Research Letters*, *33*(24), L24501. https://doi.org/10.1029/2006gl028207

Sokal, R. R., & Michener, C. D. (1958). A statistical method for evaluating systematic relationships. *University of Kansas Science Bulletin*, *38*(22), 1409–1438.

Swiss Seismological Service (SED) at ETH Zurich. (1983). National Seismic Networks of Switzerland [Dataset]. ETH Zürich. https://doi.org/10.12686/sed/networks/ch

Thelen, W. A., Allstadt, K., de Angelis, S., Malone, S. D., Moran, S. C., & Vidale, J. (2013). Shallow repeating seismic events under an alpine glacier at Mount Rainier, Washington. *Journal of Glaciology*, *59*(214), 345–356. https://doi.org/10.3189/2013JoG12J111

Thøgersen, K., Sveinsson, H., Scheibert, J., Renard, F., & Malthe-Sørenssen, A. (2019). The moment duration scaling relation for slow rupture arises from transient rupture speeds. *Geophysical Research Letters*, *46*(22), 12805–12814. https://doi.org/10.1029/2019gl084436

Thomas, A. M., Beroza, G. C., & Shelly, D. R. (2016). Constraints on the source parameters of low-frequency earthquakes on the San Andreas Fault. *Geophysical Research Letters*, *43*(4), 1464–1471. https://doi.org/10.1002/2015GL067173

Thomas, A. M., Nadeau, R. M., & Bürgmann, R. (2009). Tremor-tide correlations and near-lithostatic pore pressure on the deep San Andreas fault. *Nature*, *462*(7276), 1048–1051. https://doi.org/10.1038/nature08654

Thomason, J. F., & Iverson, N. R. (2008). A laboratory study of particle ploughing and pore-pressure feedback: A velocity-weakening mechanism for soft glacier beds. *Journal of Glaciology*, *54*(184), 169–181. https://doi.org/10.3189/002214308784409008

Uchida, N., & Bürgmann, R. (2019). Repeating earthquakes. *Annual Review of Earth and Planetary Sciences*, *47*(1), 305–332. https://doi.org/10.1146/annurev-earth-053018-060119

University of Genova. (1967). Regional Seismic Network of North Western Italy [Dataset]. International Federation of Digital Seismograph Networks. https://doi.org/10.7914/SN/GU

Vernay, M., Lafaysse, M., Hagenmuller, P., Nheili, R., Samacoïts, R., Verfaillie, D., & Morin, S. (2019). The S2M meteorological and snow cover reanalysis in the French mountainous areas (1958 – Present) [Dataset]. AERIS. https://doi.org/10.25326/37

Vincent, C., Gilbert, A., Jourdain, B., Piard, L., Ginot, P., Mikhalenko, V., et al. (2020). Strong changes in englacial temperatures despite insignificant changes in ice thickness at Dôme du Goûter glacier (Mont-Blanc area). *The Cryosphere*, *14*(3), 925–934. https://doi.org/10.5194/tc-14-925-2020

Vincent, C., & Moreau, L. (2016). Sliding velocity fluctuations and subglacial hydrology over the last two decades on Argentière glacier, Mont Blanc area. *Journal of Glaciology*, *62*(235), 805–815. https://doi.org/10.1017/jog.2016.35

Vincent, C., Soruco, A., Six, D., & Le Meur, E. (2009). Glacier thickening and decay analysis from 50 years of glaciological observations performed on Glacier d'Argentière, Mont Blanc area, France. *Annals of Glaciology*, *50*, 73–79. https://doi.org/10.3189/172756409787769500

Walter, J. I., Brodsky, E. E., Tulaczyk, S., Schwartz, S. Y., & Pettersson, R. (2011). Transient slip events from near-field seismic and geodetic data on a glacier fault, Whillans Ice Plain, West Antarctica. *Journal of Geophysical Research*, *116*(F1), F01021. https://doi.org/10.1029/2010JF001754

Walter, J. I., Svetlizky, I., Fineberg, J., Brodsky, E. E., Tulaczyk, S., Barcheck, C. G., & Carter, S. P. (2015). Rupture speed dependence on initial stress profiles: Insights from glacier and laboratory stick-slip. *Earth and Planetary Science Letters*, *411*, 112–120. https://doi.org/10.1016/j.epsl.2014.11.025

Wiens, D. A., Anandakrishnan, S., Winberry, J. P., & King, M. A. (2008). Simultaneous teleseismic and geodetic observations of the stick-slip motion of an Antarctic ice stream. *Nature*, *453*(7196), 770–775. https://doi.org/10.1038/nature06990

Winberry, J. P., Anandakrishnan, S., Wiens, D. A., & Alley, R. B. (2013). Nucleation and seismic tremor associated with the glacial earthquakes of Whillans Ice Stream, Antarctica. *Geophysical Research Letters*, *40*(2), 312–315. https://doi.org/10.1002/grl.50130

Yamada, M., Mori, J., & Matsushi, Y. (2016). Possible stick-slip behavior before the Rausu landslide inferred from repeating seismic events. *Geophysical Research Letters*, *43*(17), 9038–9044. https://doi.org/10.1002/2016GL069288

Zhao, L., Paul, A., Solarino, S., & RESIF. (2018). Seismic network XT: CIFALPS-2 temporary experiment (China-Italy-France Alps seismic transect #2) [Dataset]. RESIF – Réseau Sismologique et géodésique Français. https://doi.org/10.15778/RESIF.XT2018

Zoet, L. K., Carpenter, B., Scuderi, M., Alley, R. B., Anandakrishnan, S., Marone, C., & Jackson, M. (2013). The effects of entrained debris on the basal sliding stability of a glacier. *Journal of Geophysical Research: Earth Surface*, *118*(2), 656–666. https://doi.org/10.1002/jgrf.20052

Zoet, L. K., Ikari, M. J., Alley, R. B., Marone, C., Marone, S., Anandakrishnan, B. M., & Scuderi, M. M. (2020). Application of constitutive friction laws to glacier seismicity. *Geophysical Research Letters*, *47*(21), e2020GL088964. https://doi.org/10.1029/2020GL088964

Zoet, L. K., & Iverson, N. R. (2016). Rate-weakening drag during glacier sliding. *Journal of Geophysical Research: Earth Surface*, *121*(7), 1206–1217. https://doi.org/10.1002/2016JF003909